J. Fluid Mech. (2022), *vol*. 951, A7, doi:10.1017/jfm.2022.841

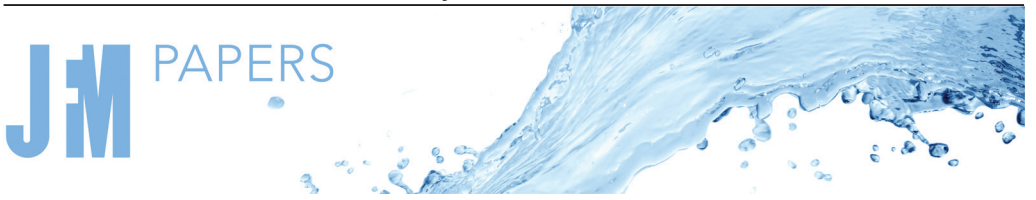

Effects of kinematic and magnetic boundary conditions on the dynamics of convection-driven plane layer dynamos

Souvik Naskar[1] **and Anikesh Pal**[1],†

[1]Department of Mechanical Engineering, Indian Institute of Technology, Kanpur 208016, India

(Received 7 February 2022; revised 21 September 2022; accepted 28 September 2022)

Rapidly rotating convection-driven dynamos are investigated under different kinematic and magnetic boundary conditions using direct numerical simulations. At a fixed rotation rate, represented by the Ekman number $Ek = 5 \times 10^{-7}$, the thermal forcing is varied from 2 to 20 times its value at the onset of convection ($\mathcal{R} = Ra/Ra_c = 2$–$20$, where Ra is the Rayleigh number), keeping the fluid properties constant ($Pr = Pr_m = 1$, where Pr and Pr_m are the thermal and magnetic Prandtl numbers). The statistical behaviour of the dynamos, including the force balance, energetics, and heat transport, depends on the boundary conditions that dictate both the boundary layer and the interior dynamics. At a fixed thermal forcing ($\mathcal{R} = 3$), the structure and strength of the magnetic field produced by the dynamos, especially near the walls, depend on both velocity and magnetic boundary conditions. Though the leading-order force balance in the bulk remains geostrophic, the Lorentz force becomes comparable to the Coriolis force inside the thermal boundary layer with no-slip, perfectly conducting conditions. In this case, a term signifying the work done by the Lorentz force in the turbulent kinetic energy (TKE) equation is found to have some components that extract energy from the velocity field to produce the magnetic field, while some other components extract energy from the magnetic field to produce TKE. However, with no-slip, pseudo-vacuum conditions, all the components of the work done by the Lorentz force perform unidirectional energy transfer to produce magnetic energy from the kinetic energy of the fluid to sustain dynamo action. We find heat transfer enhancement in the rotating dynamo convection, as compared with non-magnetic rotating convection, with the peak enhancement lying in the range $\mathcal{R} = 3$–4. For free-slip conditions, in the absence of an Ekman layer, the dynamo action may alter the heat transport significantly by suppressing the formation of large-scale vortices. However, the highest heat transfer enhancement is found at $\mathcal{R} = 3$ with no-slip, perfectly conducting walls, which can be attributed to a local magnetorelaxation of the rotational constraint due to enhanced Lorentz force inside the thermal boundary layer.

Key words: MHD turbulence, magneto convection, rotating turbulence

† Email address for correspondence: pala@iitk.ac.in

1. Introduction

The geomagnetic field acts as a shield to protect us from solar wind (Tarduno 2018) apart from directly influencing the atmosphere (Cnossen 2014), biology and evolution of life on Earth (Erdmann *et al.* 2021). Such magnetic fields of planets and stars are known to be generated by a dynamo mechanism driven by the convection of electrically conducting fluids (Rüdiger & Hollerbach 2006). In this self-sustained dynamo mechanism, the convective motion of electrically conducting fluids leads to the amplification of a small magnetic perturbation by electromagnetic induction. The induced magnetic field is then maintained against Joule dissipation by continuously converting some of the kinetic energy of the fluid to magnetic energy. A simple model of such dynamos is the Rayleigh–Bénard convection (RBC) in a plane layer between two parallel plates, heated from the bottom and cooled from the top, permeated by a magnetic field. Inclusion of global rotation in such flows can break the reflectional symmetry of the convection to induce large-scale magnetic fields (Moffatt & Dormy 2019; Tobias 2021). Non-magnetic rotating convection (RC) has been studied extensively using experiments (King *et al.* 2009; Kunnen, Geurts & Clercx 2010; King & Aurnou 2013; Ecke & Niemela 2014; Stellmach *et al.* 2014; Aurnou *et al.* 2018; Cheng *et al.* 2020), direct numerical simulations (DNS) (Schmitz & Tilgner 2010; Weiss *et al.* 2010; Stellmach *et al.* 2014; Cheng *et al.* 2015; Kunnen *et al.* 2016; Guervilly, Hughes & Jones 2017; Guzmán *et al.* 2021) and reduced-order asymptotic models (Julien *et al.* 2012*a*,*b*; Nieves, Rubio & Julien 2014; Rubio *et al.* 2014; Julien *et al.* 2016; Plumley *et al.* 2016, 2017; Maffei *et al.* 2021) to investigate the transport properties, force balance and flow structures. However, dynamical balances and heat transport in rotating dynamo convection (DC) have received less attention.

The flow and thermal field characteristics in plane layer RC serve as a classical framework for studying solar and planetary convection apart from deep convection in terrestrial oceans (Julien *et al.* 1996). Here, the convection depends primarily on the thermal forcing, the rotation rate, and the fluid properties represented by the Rayleigh number (Ra), the Ekman number (Ek) and the Prandtl number (Pr), respectively (as defined in § 2). The convection begins with steady cellular patterns when the thermal forcing exceeds a critical Rayleigh number (Ra_c), which scales as $Ek^{-4/3}$ for $Pr > 0.67$ in the limit of large rotation rates, $Ek \to 0$ (Chandrasekhar 1961). This scaling leads to higher Ra_c compared to non-rotating RBC, depicting the stabilizing action of the Coriolis force. Increasing the thermal forcing at a fixed rotation rate gives rise to distinct convection regimes with separate flow phenomenology and scaling of the transport properties. The flow regimes are classified as (i) rotation-dominated convection, (ii) rotation-affected convection, and (iii) rotation-unaffected convection, depending on the relative importance of the Coriolis force in the dynamical balance and heat transfer. The rotation-dominated convection regime is characterized by a geostrophic balance between Coriolis and pressure forces, whereas inertial effects break this balance in the rotation-affected convection regime at higher thermal forcing. The dependence on the rotation rate is diminished at even higher forcing for the rotation-unaffected regime with heat transfer behaviour similar to RBC (see Kunnen (2021) for details). Even the rotation-dominated geostrophic convection regime can be divided into sub-regimes with distinct flow structures, such as (in the order of increasing thermal forcing) cells, transient Taylor columns, plumes, and large-scale vortices (LSV) in geostrophic turbulence (Julien *et al.* 2012*b*; Nieves *et al.* 2014; Kunnen *et al.* 2016). Most of these flow features have been confirmed by laboratory experiments in rotating cylinders (Kunnen *et al.* 2010; Cheng *et al.* 2015). In the simulations, the flow features may also depend on the boundary conditions imposed on the plates. For example, LSV formation in geostrophic turbulence is shifted to higher rotation rates with

no-slip boundary conditions as compared to the free-slip boundary conditions at a fixed thermal forcing (Guzmán *et al.* 2020), as no-slip boundaries can suppress the formation (Stellmach *et al.* 2014; Kunnen *et al.* 2016). Though the regime transition with thermal forcing is found to be independent of boundary conditions (Kunnen *et al.* 2016), the force balance and heat transport behaviour in RC depends on the kinematic boundary conditions.

The classical RBC between parallel plates can be separated into two regions: (i) the boundary layer regions with high thermal and velocity gradients near the plates, and (ii) the well-mixed bulk region in the interior. In the absence of rotation, the heat transport is throttled by the presence of boundary layers, with the Nusselt number (Nu, a non-dimensional measure of heat transfer defined in (2.10)) scaling as $Ra^{1/3}$ with the thermal forcing (Plumley & Julien 2019; Iyer *et al.* 2020). The thermal behaviour of plane layer RC in the rotation-dominated regime is diametrically opposite, with the bulk rather than the boundary layer constraining the convective heat transport. For large rotation rates ($Ek \to 0$), the heat transfer should follow the diffusion-free scaling $Nu \sim Ra^{3/2}$ irrespective of the boundary conditions (Julien *et al.* 2012*a*). Experimental difficulties in maintaining turbulence at small Ek, and the computational challenges pertaining to the spatio-temporal resolution requirement restrict the demonstration of this scaling in a laboratory or DNS with no-slip boundaries. Instead, the Ekman pumping near the thin boundary layers significantly enhances the heat transport even at low Ekman numbers $Ek \approx 10^{-8}$ (Kunnen *et al.* 2010; Stellmach *et al.* 2014). This results in a steeper heat transport scaling $Nu \sim Ra^{3}$, when no-slip conditions are used rather than free-slip conditions at the boundaries. Reduced-order models with parametrized Ekman pumping corroborate these scaling predictions (Stellmach *et al.* 2014; Plumley *et al.* 2016, 2017). The presence of no-slip walls, with the associated Ekman pumping effect, can significantly enhance vertical velocities, even in the interior, because of the enhanced momentum flux from the boundary towards the bulk. The viscous and inertial force magnitudes near the walls also increase by one order of magnitude compared to their bulk values near the no-slip boundaries, leading to increased ageostrophy (Guzmán *et al.* 2021).

Motivated by the boundary layer effects on plane layer RC, we intend to investigate the boundary layer dynamics in DC under different combinations of kinematic and magnetic boundary conditions. For rotating DC, the magnetic Prandtl number (Pr_m) appears as an extra parameter that decides the growth and saturation of the magnetic field (Tobias, Cattaneo & Boldyrev 2012; Tobias 2021). Such plane layer convection of electrically conducting fluids was shown to induce dynamo action in early analytical (Childress & Soward 1972; Soward 1974; Fautrelle & Childress 1982) and numerical (Meneguzzi & Pouquet 1989) studies. Using this plane layer model with no-slip and perfectly conducting boundaries, St Pierre (1993) demonstrated subcritical dynamo action at $Ek = 5 \times 10^{-6}$, with the magnetic field concentrated near the plates. Thelen & Cattaneo (2000) studied the effect of perfectly conducting, perfectly insulating and pseudo-vacuum magnetic boundary conditions on dynamo action. These boundary conditions were found to dictate the strength and structure of the magnetic field near the plates, though the bulk behaviour was independent of the boundary conditions. Stellmach & Hansen (2004) used free-slip, perfectly conducting boundaries to study rapidly rotating ($Ek = 10^{-4}$–5×10^{-7}) weakly nonlinear DC, and reported strongly time-dependent flow and magnetic field behaviour, with cyclic variation between small- and large-scale structures. These particular boundary conditions facilitate comparison of the dynamo behaviour with analytical models (Childress & Soward 1972; Soward 1974). They reported strongly time-dependent flow and magnetic field behaviour, with cyclic variation between small- and large-scale

structures. Tilgner (2012, 2014) reported a transition between large-scale field generation governed by flow helicity to small-scale field generation driven by field stretching. The transition happens at $Re_m\, Ek^{1/3} \approx 10.7$ (where Re_m is the magnetic Reynolds number signifying the relative strength of electromagnetic induction over Ohmic diffusion), for perfectly conducting boundaries irrespective of the kinematic condition (no-slip or free-slip). Large-scale-vortex-driven dynamos were demonstrated by Guervilly, Hughes & Jones (2015) and Guervilly *et al.* (2017), generating a large-scale magnetic field. In the absence of a magnetic field, these vortices lead to the reduction of heat transfer between the plates (Guervilly, Hughes & Jones 2014). However, a small-scale magnetic field may suppress the formation of LSV at sufficiently high $Re_m \gtrsim 550$ (Guervilly *et al.* 2017). Interestingly, Yan & Calkins (2022*b*) has recently demonstrated the existence of large-scale fields in rapidly rotating DC with a dominant mean magnetic field for $Re_m\, Ek^{1/3} \lesssim O(1)$, without the presence of large flow helicity or LSV. Asymptotically reduced DC models (vanishingly small inertia and viscous forces with respect to the Coriolis force), with a leading-order geostrophic balance, were studied by Calkins *et al.* (2015), revealing four distinct dynamo regimes with separate scaling for the magnetic to kinetic energy density ratios (Calkins 2018). RBC-driven dynamos have been studied by Yan, Tobias & Calkins (2021), who reported heat transfer scaling similar to non-rotating convection. Yan & Calkins (2022*a*) have reported the force balance, heat transport and scaling of the flow properties in rapidly rotating DC with free-slip, pseudo-vacuum boundary conditions. The scaling of the transport properties was found to be consistent with the asymptotic theory of Calkins *et al.* (2015) and Calkins (2018). Recently, Kolhey, Stellmach & Heyner (2022) have studied the effect of thermal, kinematic and magnetic boundary conditions in DC in the geostrophic turbulent regime. The magnetic field topology was found to depend on the choice of magnetic boundary conditions. Nevertheless, the dependence of the heat transfer, force balance and energetics on the boundary conditions for varying flow regimes remains open for exploration.

In the present study, we perform DNS of convection-driven dynamos, in the rotation-dominated regime, with varying thermal forcing subjected to different boundary conditions. Our simulations of plane layer RC, with no-slip and free-slip kinematic boundary conditions, serve as references to study the dynamo behaviour at four combinations of boundary conditions (combinations of no-slip or free-slip as velocity boundary conditions with perfectly conducting or pseudo-vacuum magnetic boundary conditions). The statistical characteristics of the dynamo, along with the existing force balance in the system, are found to depend on the kinematic and magnetic boundary conditions, both in the bulk and in the boundary layer region. Heat transfer behaviour was also found to be strongly dependent on the imposed conditions at the plates. The governing equations with the boundary conditions are detailed in § 2. The statistical behaviour of the flow and magnetic field is presented in § 3.1. In §§ 3.2 and 3.3, we present the force balance and energy budget in the dynamos. Finally, we look into the heat transport behaviour in § 3.4, and summarize our findings in § 4.

2. Method

2.1. *Governing equations*

In the present study, rapidly rotating DC in a three-dimensional Cartesian layer of incompressible, electrically conducting, Boussinesq fluid is considered. The horizontal layer is kept between two parallel plates at distance d and temperature difference

ΔT, where the lower plate is hotter than the upper plate. The system rotates with a constant angular velocity $\boldsymbol{\Omega} = \Omega \hat{e}_3$ about the vertical axis, anti-parallel to the gravity $\boldsymbol{g} = -g\hat{e}_3$. The electrically conducting Newtonian fluid has density ρ, kinematic viscosity ν, thermal diffusivity κ, adiabatic volume expansion coefficient α, magnetic permeability μ, electrical conductivity σ, and magnetic diffusivity η. The layer depth d and temperature difference ΔT are the natural choices for length and temperature scales, whereas $u_f = \sqrt{g\alpha\,\Delta T\, d}$, and $\sqrt{\rho\mu}\,u_f$ are chosen to be the velocity (Guzmán *et al.* 2021) and magnetic field scales. The non-dimensional governing equations for the velocity field u_i, temperature field θ, and magnetic field B_i are expressed as follows:

$$\frac{\partial u_j}{\partial x_j} = \frac{\partial B_j}{\partial x_j} = 0, \tag{2.1}$$

$$\frac{\partial u_i}{\partial t} + u_j \frac{\partial u_i}{\partial x_j} = -\frac{\partial p}{\partial x_i} + \frac{1}{Ek}\sqrt{\frac{Pr}{Ra}}\,\epsilon_{ij3}\,u_j\,\widehat{e_3} + B_j \frac{\partial B_i}{\partial x_j} + \theta\delta_{i3} + \sqrt{\frac{Pr}{Ra}}\,\frac{\partial^2 u_i}{\partial x_j\,\partial x_j}, \tag{2.2}$$

$$\frac{\partial \theta}{\partial t} + u_j \frac{\partial \theta}{\partial x_j} = \frac{1}{\sqrt{Ra\,Pr}}\,\frac{\partial^2 \theta}{\partial x_j\,\partial x_j}, \tag{2.3}$$

$$\frac{\partial B_i}{\partial t} + u_j \frac{\partial B_i}{\partial x_j} = B_j \frac{\partial u_i}{\partial x_j} + \sqrt{\frac{Pr}{Ra}}\,\frac{1}{Pr_m}\,\frac{\partial^2 B_i}{\partial x_j\,\partial x_j}. \tag{2.4}$$

The definitions of the four non-dimensional parameters – namely Rayleigh number (Ra), Ekman number (Ek), thermal and magnetic Prandtl numbers (Pr and Pr_m) – are given as follows:

$$Ra = \frac{g\alpha\,\Delta T\, d^3}{\kappa\nu}, \quad Ek = \frac{\nu}{2\Omega d^2}, \quad Pr = \frac{\nu}{\kappa}, \quad Pr_m = \frac{\nu}{\eta}. \tag{2.5a–d}$$

In the horizontal directions (x_1, x_2), periodic boundary conditions are applied. As we aim to study the effect of Ekman layer dynamics on the dynamo convection, both no-slip and free-slip boundary conditions are implemented in the vertical direction (x_3), as follows:

$$\left.\begin{aligned} u_1 = u_2 = u_3 = 0 \quad &\text{at } x_3 = \pm 1/2 \quad \text{(no-slip)}, \\ \frac{\partial u_1}{\partial x_3} = \frac{\partial u_2}{\partial x_3} = 0,\, u_3 = 0 \quad &\text{at } x_3 = \pm 1/2 \quad \text{(free-slip)}. \end{aligned}\right\} \tag{2.6}$$

Isothermal boundary conditions with unstable temperature gradient are imposed to drive convection as follows:

$$\theta = 1/2 \text{ at } x_3 = -1/2, \quad \theta = -1/2 \text{ at } x_3 = 1/2. \tag{2.7a,b}$$

For the magnetic field, both perfectly conducting and pseudo-vacuum conditions are implemented to compare the resulting magnetic field structure. For a perfectly conducting boundary, the field is constrained to be horizontal at the wall (Cattaneo & Hughes 2006). The pseudo-vacuum conditions (Thelen & Cattaneo 2000; Kolhey *et al.* 2022), where the field is purely vertical at the boundaries, are used to approximate insulating conditions

(Jones & Roberts 2000):

$$\left.\begin{aligned} \frac{\partial B_1}{\partial x_3} = \frac{\partial B_2}{\partial x_3} = B_3 = 0 \quad \text{at}\, x_3 = \pm 1/2 \quad (\text{perfectly conducting}), \\ B_1 = B_2 = \frac{\partial B_3}{\partial x_3} = 0 \quad \text{at}\, x_3 = \pm 1/2 \quad (\text{pseudo-vacuum}). \end{aligned}\right\} \tag{2.8}$$

2.2. *Simulation details*

The governing equations (2.1)–(2.4) are solved in a cubic domain with a unit side length, using a finite difference method. The geometrical details and numerical algorithms are presented in Naskar & Pal (2022). We perform all the simulations at constant rotation rate and constant fluid properties by varying the thermal forcing and boundary conditions. The thermal forcing is represented by the convective supercriticality $\mathcal{R} = Ra/Ra_c$, where Ra_c is the minimum value of Ra required to start steady RC (Chandrasekhar 1961). In this study, we have used the values of critical Rayleigh number for non-magnetic convection as $Ra_c = 8.6Ek^{-4/3}$ for free-slip boundaries (Chandrasekhar 1961) and $Ra_c = 7.6Ek^{-4/3}$ for no-slip boundaries (King, Stellmach & Aurnou 2012; Kunnen 2021). It should be noted here that the prefactors in these expressions of Ra_c are different from those reported in our previous study due to the difference in the definition of Ekman number in (2.5*b*). We choose the values of $\mathcal{R} = 2, 2.5, 3, 4, 5, 10, 20$, Ekman number $Ek = 5 \times 10^{-7}$ and the Prandtl numbers $Pr = Pr_m = 1$ for the present simulations. To investigate dynamo action for different boundary conditions, we perform six simulations at each value of $\mathcal{R}$: (*a*) non-magnetic RC with no-slip (NS) and free-slip (FS) boundary conditions, and (*b*) rotating DC subjected to the combinations of kinematic (no-slip or free-slip) and magnetic (perfectly conducting or pseudo-vacuum) boundary conditions, abbreviated as NSC, FSC, NSV and FSV. The simulation inputs and diagnostic parameters are summarized in tables 1–4. The computational domain, with an aspect ratio of unity, is about 26 times larger than the critical wavelength at the onset of RC ($\lambda_c = 4.8158Ek^{1/3}$) in the horizontal directions (Chandrasekhar 1961). Therefore, we can ensure the statistical convergence of all the diagnostic properties (Yan & Calkins 2022*a*) presented in tables 1–4. A mesh with $1024 \times 1024 \times 256$ grid points is used for all the simulations, with uniform spacing in the horizontal and grid clustering in the vertical direction to resolve the boundary layers. The solver has been validated extensively for studies on rotating stratified flow (Pal & Chalamalla 2020), and various transitional and turbulent shear flows (Brucker & Sarkar 2010; Pal, de Stadler & Sarkar 2013; Pal & Sarkar 2015; Pal 2020). Details of the grid resolution and validation studies are reported in a previous study (Naskar & Pal 2022). The scaled values of the buoyancy flux $\langle \mathcal{B} \rangle^* = \langle u_3 \theta \rangle \times 10^4$ and the total dissipation $\langle \epsilon \rangle^* = \langle \epsilon_v + \epsilon_j \rangle \times 10^4$ in tables 1–4 indicate sufficient resolution for all the simulations, as the grid can capture most of the energetic scales. It should be noted that the combination of the non-dimensional numbers appearing before the Coriolis term in the momentum equation (2.2) is the inverse of the convective Rossby number $Ro_C = Ek(Ra/Pr)^{1/2}$ used frequently in the literature on rapid RC (Aurnou, Horn & Julien 2020). For all our simulations, the convective Rossby number $Ro_C \ll 1$ indicates the rapid RC regime, as shown in tables 1–4. The reduced Rayleigh number $\widetilde{Ra} = Ra\, Ek^{4/3}$ is another important parameter presented in these tables to compare against the literature on rapid RC (Julien *et al.* 2012*a*; King *et al.* 2012; Calkins 2018).

$\mathcal{R}$	$\widetilde{Ra}$	Ro_C	Re_m	Λ_{tr}	Λ_V	Λ_T	$\bar{M}/M$	$\frac{Nu}{Nu_0}$	$\frac{\langle\epsilon_v\rangle}{\langle\epsilon_0\rangle}$	$\frac{\langle\epsilon_j\rangle}{\langle\epsilon\rangle}$	$\langle\mathcal{B}\rangle^*$	$-\langle\epsilon\rangle^*$	τ	τ_0
2	15.2	0.031	729	0.109	0.038	0.005	0.3994	0.73	0.50	0.32	0.562	0.542	1.171	—
2.5	19.0	0.035	1327	0.258	0.011	0.292	0.0603	1.26	0.94	0.34	1.955	1.934	1.027	—
3	22.8	0.038	2012	0.516	0.071	0.617	0.0040	1.72	1.44	0.36	3.566	3.459	0.933	—
4	30.4	0.044	2284	0.842	0.087	0.555	0.0033	1.49	1.23	0.38	3.737	3.694	0.848	—
5	38.0	0.049	2660	1.199	0.129	0.462	0.0029	1.43	1.08	0.39	3.675	3.661	0.827	—
10	76.0	0.069	4203	1.871	0.132	0.214	0.0006	1.17	0.85	0.34	3.902	3.818	0.784	—
20	152.0	0.098	7642	6.643	0.183	0.167	0.0003	1.14	0.82	0.39	5.141	4.980	0.930	—

Table 1. Statistics of the dynamo simulations with NSC boundary conditions.

$\mathcal{R}$	$\widetilde{Ra}$	Ro_C	Re_m	Λ_{tr}	Λ_V	Λ_T	$\bar{M}/M$	$\frac{Nu}{Nu_0}$	$\frac{\langle\epsilon_v\rangle}{\langle\epsilon_0\rangle}$	$\frac{\langle\epsilon_j\rangle}{\langle\epsilon\rangle}$	$\langle\mathcal{B}\rangle^*$	$-\langle\epsilon\rangle^*$	τ	τ_0
2	15.2	0.031	682	0.295	0.009	0.011	0.1617	0.95	0.69	0.40	0.754	0.724	1.302	1.058
2.5	19.0	0.035	1403	0.311	0.044	0.043	0.0043	1.00	1.20	0.20	1.529	1.516	1.072	1.071
3	22.8	0.038	2044	0.439	0.095	0.097	0.0015	1.41	1.26	0.25	2.901	2.969	1.034	1.046
4	30.4	0.044	2212	0.889	0.055	0.112	0.0008	1.24	0.95	0.36	3.063	3.050	0.903	0.986
5	38.0	0.049	2491	1.063	0.038	0.159	0.0007	1.23	0.92	0.36	3.153	3.131	0.816	0.958
10	76.0	0.069	3748	2.934	0.033	0.269	0.0006	1.10	0.71	0.42	3.670	3.548	0.735	1.102$^{\#}$
20	152.0	0.098	6422	7.995	0.021	0.371	0.0005	1.09	0.82	0.41	6.185	6.042	0.707	1.341$^{\#}$

Table 2. Statistics of the dynamo simulations with NSV boundary conditions.

$\mathcal{R}$	$\widetilde{Ra}$	Ro_C	Re_m	Λ_{tr}	Λ_V	Λ_T	$\bar{M}/M$	$\frac{Nu}{Nu_0}$	$\frac{\langle\epsilon_v\rangle}{\langle\epsilon_0\rangle}$	$\frac{\langle\epsilon_j\rangle}{\langle\epsilon\rangle}$	$\langle\mathcal{B}\rangle^*$	$-\langle\epsilon\rangle^*$	τ	τ_0
2	17.4	0.033	641	0.218	0.001	0.001	0.1853	0.98	0.98	0.07	0.345	0.343	1.174	1.351
2.5	21.7	0.037	950	0.326	0.002	0.003	0.0173	1.00	0.97	0.03	0.524	0.520	1.234	1.350
3	26.1	0.041	1176	0.437	0.003	0.005	0.0061	1.08	1.02	0.01	0.585	0.581	1.171	1.414
4	34.8	0.047	2087	0.503	0.004	0.006	0.0020	1.44	1.04	0.34	1.812	1.753	1.019	2.960$^{\#}$
5	43.5	0.052	2562	0.744	0.005	0.013	0.0019	1.42	1.02	0.35	2.248	2.162	0.953	3.054$^{\#}$
10	87.0	0.074	3957	2.072	0.007	0.037	0.0018	1.02	0.74	0.39	2.883	2.718	0.825	7.755$^{\#}$
20	174.0	0.105	7249	6.570	0.009	0.091	0.0008	0.98	0.73	0.42	4.482	4.261	0.802	4.050$^{\#}$

Table 3. Statistics of the dynamo simulations with FSC boundary conditions.

2.3. *Turbulence statistics*

For moderate to high $Re_m \geqslant O(10\text{–}100)$, the system can induce its own magnetic field with a wide range of length and time scales. In such cases, it is worthwhile to decompose the magnetic field into mean and fluctuating parts following the developments in mean field electrodynamics (Cattaneo & Hughes 2006). Therefore, we perform Reynolds decomposition on all the variables such that

$$\left.\begin{aligned} \phi(x, y, z, t) &= \bar{\phi}(z, t) + \phi'(x, y, z, t), \\ \bar{\phi}(z, t) &= \int_{A_h} \phi(x, y, z, t)\, \mathrm{d}x\, \mathrm{d}y. \end{aligned}\right\} \tag{2.9}$$

$\mathcal{R}$	$\widetilde{Ra}$	Ro_C	Re_m	Λ_{tr}	Λ_V	Λ_T	$\bar{M}/M$	$\frac{Nu}{Nu_0}$	$\frac{\langle\epsilon_v\rangle}{\langle\epsilon_0\rangle}$	$\frac{\langle\epsilon_j\rangle}{\langle\epsilon\rangle}$	$\langle\mathcal{B}\rangle^*$	$-\langle\epsilon\rangle^*$	τ	τ_0
2	17.4	0.033	460	0.026	0.027	0.017	0.0125	0.64	0.86	0.36	0.336	0.336	2.661	—
2.5	21.7	0.037	1056	0.034	0.030	0.019	0.0066	0.99	0.98	0.31	0.521	0.519	1.395	—
3	26.1	0.041	1414	0.047	0.036	0.019	0.0033	1.34	1.23	0.38	0.759	0.754	1.289	—
4	34.8	0.047	1858	0.999	0.043	0.029	0.0014	1.26	0.65	0.44	1.485	1.392	0.980	—
5	43.5	0.052	2311	2.0726	0.107	0.044	0.0013	1.23	0.64	0.50	2.101	1.995	0.886	—
10	87.0	0.074	3475	57.122	1.187	0.186	0.0011	1.19	0.32	0.78	4.323	4.192	0.917	—
20	174.0	0.105	6332	99.573	1.367	0.305	0.0009	1.13	0.33	0.72	5.766	5.712	0.848	—

Table 4. Statistics of the dynamo simulations with FSV boundary conditions. In tables 1–4, subscript '0' represents the properties for non-magnetic RC simulations. Such RC simulations with LSV are indicated by # in the last column.

Here, A_h is the horizontal area of integration of the flow variables $\phi = \{u_i, p, \theta, B_i\}$. The root-mean-square (r.m.s.) values are calculated as $\phi_{rms} = (\overline{\phi'^2})^{1/2}$. The energy budget for the turbulent kinetic energy (TKE) K, as derived from the momentum equation (2.2) by utilizing (2.9), is presented in Appendix A.

We compare our simulations in terms of the heat transfer, represented by the Nusselt number(Nu). This is defined as the ratio of total heat flux to the conductive heat flux transferred from the bottom plate to the top plate:

$$Nu = \frac{qd}{k\,\Delta T} = 1 + \sqrt{Ra\,Pr}\,\langle\mathcal{B}\rangle. \tag{2.10}$$

Here, $\langle\phi\rangle = \int_0^1 \bar{\phi}\,\mathrm{d}x_3$ denotes the average over the entire volume, q represents the total heat flux, and $\mathcal{B}$ stands for the vertical buoyancy flux (see (A2c)). Subscript '0' is used to represent the properties without magnetic field (NS and FS cases) in the rest of this paper. All the statistics presented here are averaged in time for at least 100 free-fall time units d/u_f, after the simulations settle in a statistically stationary state.

3. Results

Naskar & Pal (2022) performed DNS of rapidly rotating dynamos with no-slip boundary conditions and reported a significant enhancement (72 %) in heat transfer as compared to non-magnetic RC at $\mathcal{R} = 3$. An increase in the Lorentz force near the boundaries was found to be the reason for this enhanced heat transport. Owing to this interesting behaviour, we study the statistical details, force balance and energy budget of the dynamos at $\mathcal{R} = 3$ subjected to different boundary conditions. To further understand the changes in the dynamo behaviour with $\mathcal{R}$, we have tabulated the volume-averaged statistics in tables 1–4.

3.1. *Statistical details of the dynamos*

In this section, we discuss the statistical behaviour of the velocity, temperature and magnetic field of the dynamos subjected to different boundary conditions at $\mathcal{R} = 3$. In figure 1(a), the r.m.s. horizontal velocity is presented. To clarify the near-wall variation,

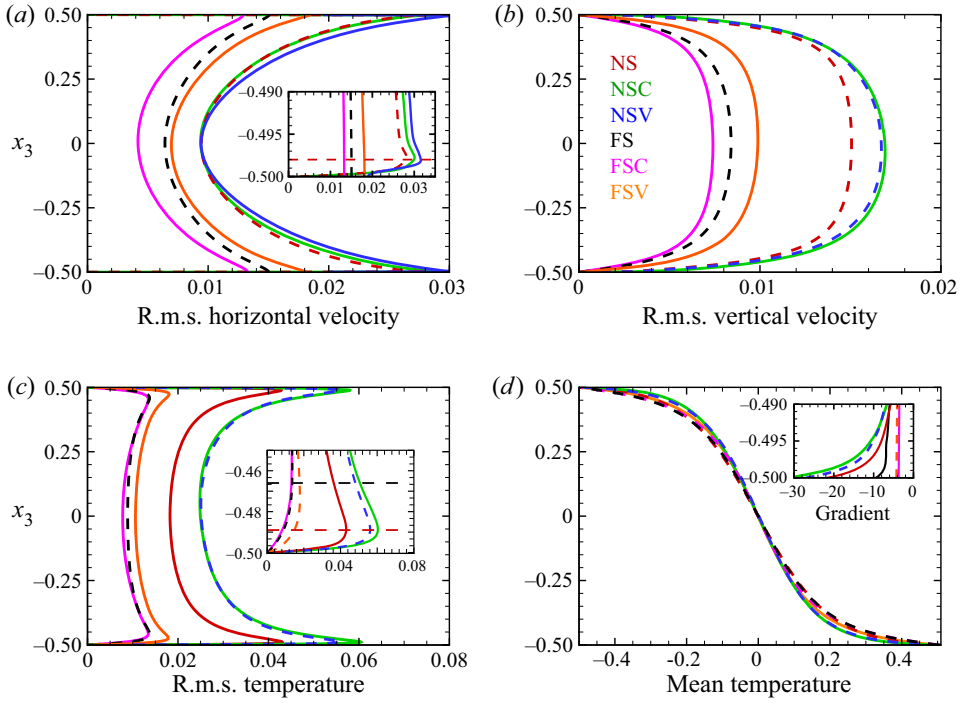

Figure 1. Vertical variation of the r.m.s. quantities: (*a*) horizontal velocity $u_{1,rms}$; (*b*) vertical velocity $u_{3,rms}$; (*c*) r.m.s. temperature $\theta_{r.m.s.}$; (*d*) mean temperature $\bar{\theta}$ at $\mathcal{R} = 3$. All the quantities are averaged in time and in the horizontal directions. Dashed lines are used as needed for improving the clarity of the plots.

we have included a magnified inset. At this point, it is important to distinguish between the well-mixed bulk region in the interior and the boundary layer region with high gradients near the plates. Therefore, we define the thermal boundary layer as the region near the plates where temperature gradients are high, and its thickness (δ_T) is evaluated as the distance from the wall, where the r.m.s. value of temperature reaches a maximum (King *et al.* 2009). Furthermore, when the no-slip condition is imposed, the viscous effects are confined within a thin Ekman layer, defined as the distance of the maximum horizontal r.m.s. velocity from the wall, δ_{Ek}. The edge of the Ekman boundary layer for the no-slip cases at $x_3 = -0.498$, as marked with a horizontal red dashed line in the inset in figure 1(*a*), remains independent of the magnetic boundary conditions. In figure 1(*a*), the horizontal velocities in the bulk for NS and NSC cases overlap, whereas the profiles inside the Ekman layer are independent of magnetic boundary conditions. For the no-slip boundary condition, the horizontal velocity can be seen to be higher than that of the free-slip boundaries, both in the bulk and near the boundaries. A similar behaviour is observed for the r.m.s. vertical velocity and temperature fluctuations in figures 1(*b*) and 1(*c*), respectively.

The vertical variation of the r.m.s. velocities can be understood from the Ekman pumping mechanism (Guzmán *et al.* 2021). The velocity magnitudes around a plume site, as depicted in figure 2, can provide further insight into this phenomenon. Here, the conical plume sites can be recognized from the temperature isosurface $\theta = 0.45$ near the lower boundary in figure 2(*a*). The horizontal convergence (or divergence) of fluid at the sites of the vortical plumes (figure 2*b*) enhances the horizontal velocity near the wall with

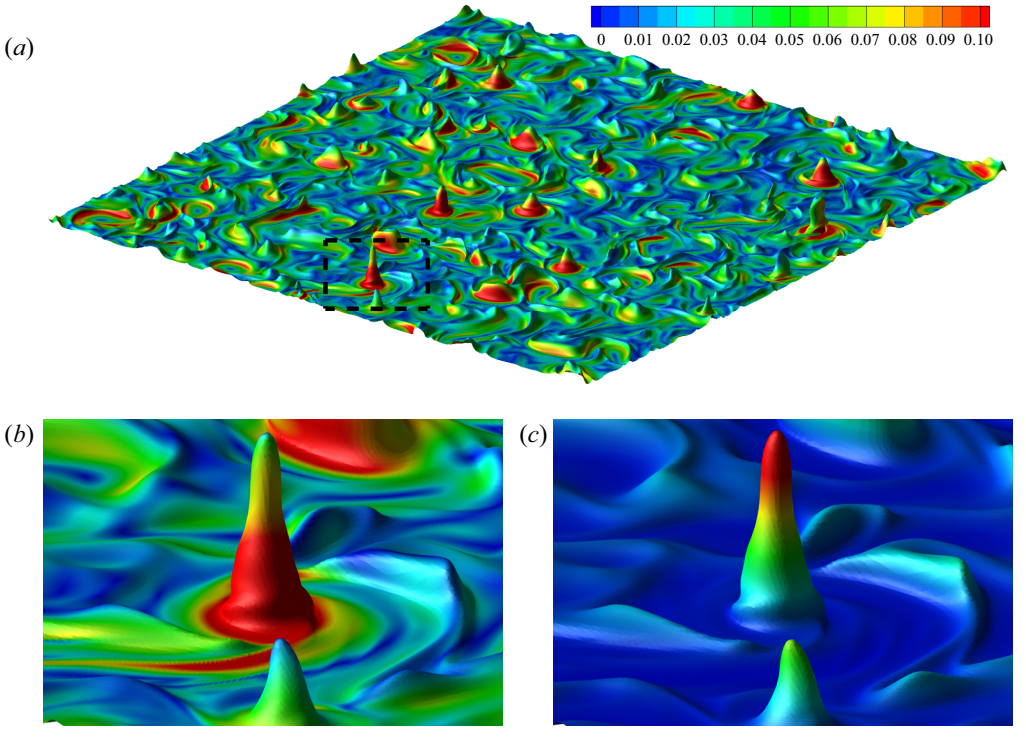

Figure 2. (*a*) Plume sites visualized by an isosurface of the instantaneous temperature field with $\theta = 0.45$, coloured by the horizontal velocity for the NSC case at $\mathcal{R} = 3$. A typical plume site in (*a*), as marked by the dashed rectangle, has been magnified and coloured by horizontal and vertical velocities in (*b*,*c*) respectively.

the no-slip boundary condition compared to the free-slip cases in figure 1(*a*). This fluid then gains vertical acceleration towards the bulk, resulting in higher vertical velocities (figure 2*c*), as plotted in figure 1(*b*). Ekman pumping induced by the no-slip boundaries is known to enhance momentum and heat transport (Stellmach *et al.* 2014), and is the reason for the enhanced r.m.s. velocities and temperature fluctuations, especially near the boundaries.

Furthermore, in the inset of figure 1(*c*), the thermal boundary layer thickness (δ_T) for the free-slip boundaries (horizontal black dashed line) is about three times higher than the no-slip boundaries (horizontal red dashed line). The thermal fluctuations are enhanced with no-slip boundary conditions, with maximum r.m.s. fluctuation shifting towards the wall. It is noteworthy that changing the boundary conditions can significantly modulate the bulk behaviour apart from the boundary layer dynamics. Also, the effects of changing the kinematic boundary condition on the velocity and thermal fields are more prominent than the magnetic conditions. The mean temperature profile shows a higher temperature gradient near the bottom wall for no-slip conditions (see the inset in figure 1*d*), with the highest vertical gradient for the NSC case indicating the highest heat transfer from the wall among all the cases at $\mathcal{R} = 3$ (see § 3.4 for detailed discussion). However, the mean temperature profile and its gradient at the mid-plane remain nearly independent of boundary conditions.

In the present simulations, the magnetic Reynolds number $Re_m = Re\,Pr_m = u_\tau d/\eta$ (where $u_\tau = u_f \langle 2K \rangle^{1/2}$ is the turbulent velocity scale) has the same value with the

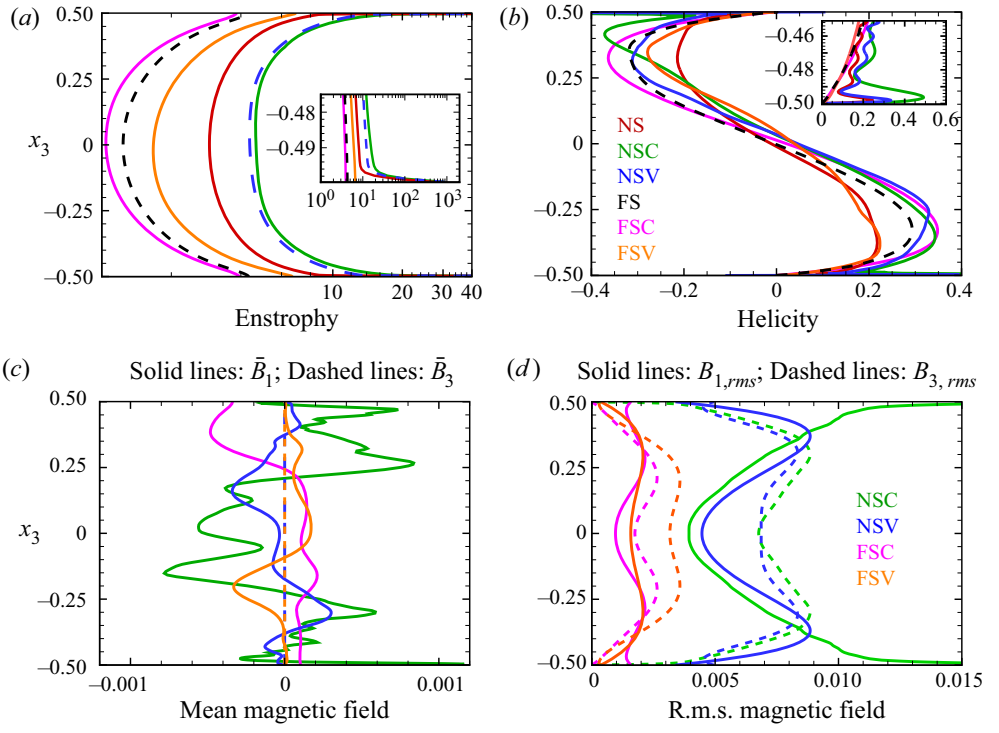

Figure 3. Vertical variation of the r.m.s. quantities: (*a*) enstrophy, (*b*) relative helicity, (*c*) mean magnetic field, (*d*) r.m.s. magnetic field at $\mathcal{R} = 3$. All the quantities are averaged in time and in the horizontal directions. The mean and r.m.s. magnetic fields in figures (*c*) and (*d*) are plotted using solid lines for x_1-direction and dashed line for x_3-direction.

Reynolds number Re, for $Pr_m = 1$ (see tables 1–4). The Reynolds number increases by an order of magnitude in the range $\mathcal{R} = 2$–20, indicating increased velocity fluctuations with thermal forcing, irrespective of boundary conditions. The r.m.s. temperature fluctuations also increase monotonically with increased thermal forcing (figure not presented). The decreasing rotational constraint with increasing $\mathcal{R}$ leads to decreasing effect of Ekman pumping on the velocity and temperature field. Therefore, the differences between r.m.s. velocity and temperature magnitudes with no-slip and free-slip conditions diminish with increasing $\mathcal{R}$. We find LSV in the regime of geostrophic turbulence for FS cases (see tables 2–3 and § 3.4 for details). With this flow structure, the horizontal velocity becomes higher than for all the other cases.

Apart from the velocity and thermal fields, we look into the effect of boundary conditions on the enstrophy, relative helicity and the magnetic field. The vertical variations of horizontally averaged enstrophy, relative helicity, mean and r.m.s. magnetic field strengths are depicted in figures 3(*a–d*), respectively. In turbulent dynamos, the dynamical alignment of magnetic field lines (Tobias 2021) occurs around the edges of vortices. A measure of the strength of the vortical elements in the flow is given by the enstrophy $Ek_\omega = 1/2\,\overline{\omega_i\omega_i}$. The strength of the vortices can decide the extent to which they can deform the magnetic field lines around them, and therefore can be correlated with the local Lorentz force magnitude (Naskar & Pal 2022). The vorticity fluctuations are enhanced in the bulk, as depicted by the enstrophy, with a more than two orders of magnitude jump near the boundaries (see the inset in figure 3*a*). The strengths of the vortices are enhanced

due to Ekman pumping near the wall. The presence of the energetic vortices near the wall may significantly alter the boundary layer dynamics and the associated heat transfer characteristics of a dynamo compared to the same without the presence of an Ekman layer with free-slip boundaries (Naskar & Pal 2022).

Another important quantity is the kinetic helicity of the flow, which can induce large-scale mean fields in a dynamo (Tilgner 2012). The relative kinetic helicity $\mathcal{H}_r = \overline{u_i\omega_i}/2(KE_\omega)^{1/2}$ exhibits the well-known spatial segregation in the vertical direction, as expected in RC, with negative and positive helicity dominating in the bottom and top halves of the domain, respectively (Cattaneo & Hughes 2006; Schmitz & Tilgner 2010). Helicity is enhanced by the presence of the wall, where the thermal plumes departing from the boundary layer towards the bulk are spun up by the Coriolis force, due to Ekman pumping (Schmitz & Tilgner 2010). This phenomenon results in a strong correlation between local velocity and vorticity that leads to a peak of relative kinetic helicity near the wall, as shown in the inset in figure 3(*b*). However, in the bulk, the relative helicity magnitude remains similar for all the dynamo simulations.

Additionally, we look into the effect of boundary conditions on the strength and structure of the magnetic field produced by the dynamos. The horizontally averaged mean magnetic field is plotted in figure 3(*c*), which illustrates the dependence on magnetic boundary conditions, even in the bulk. NSC conditions lead to the highest mean field magnitude among all the cases. It should be noted here that for perfectly conducting boundaries, the vertical component of the mean magnetic field, $\bar{B}_3$, is identically zero by the definition of averages (2.9) and the solenoidal field condition (2.1), so that the mean field remains horizontal. Conversely, the mean field is three-dimensional with a purely vertical field at the boundaries for pseudo-vacuum conditions. However, at $\mathcal{R} = 3$, the mean vertical field remains small compared to the horizontal field for NSV and FSV conditions in figure 3(*c*). We find that the vertical averages of $\bar{B}_1$ and $\bar{B}_2$ are two orders of magnitude smaller than the maximum mean field strength for NSC and FSC boundary conditions. Jones & Roberts (2000) also demonstrate analytically that for perfectly conducting boundaries, the vertical averages of the mean magnetic fields are zero. However, NSV and FSV boundaries do not satisfy this condition.

In contrast to the mean-field, the fluctuating part of the magnetic field is always three-dimensional, with all components non-zero except at the wall. The r.m.s. values of the fluctuating horizontal and vertical magnetic fields are plotted in figure 3(*d*). For $\mathcal{R} = 3$, the fluctuating magnetic field is approximately one order of magnitude stronger than the mean magnetic field. However, lower thermal forcing can generate strong, large-scale mean magnetic fields, as reported in earlier studies (Stellmach & Hansen 2004; Tilgner 2012; Naskar & Pal 2022). Dynamos with no-slip boundary conditions lead to higher r.m.s. field strength than that with free-slip boundaries. For NSC conditions, a large horizontal r.m.s. field magnitude can be observed near the boundaries. The stretching of the magnetic field lines by the strong vortices near the wall results in an increase in the r.m.s. field strength. As the magnetic field has to remain parallel to a perfectly conducting surface, it remains trapped near the walls, leading to a build-up of the magnetic field strength (St Pierre 1993). Recently, the DNS of Kolhey *et al.* (2022) have confirmed this build-up of the field for NSC conditions that creates a stringent resolution requirement near the boundaries. The overall structure and magnitude of the magnetic field, both in the bulk and near the boundaries, are strongly dependent on the combination of kinematic and magnetic boundary conditions for all $\mathcal{R}$.

In tables 1–4, the traditional Elsasser number $\Lambda_{tr} = \sigma B_\tau^2/2\rho\Omega = 2\,Ra\,EM\,Pr_m/Pr$ provides a non-dimensional measure of the magnetic field strength, where $M =$

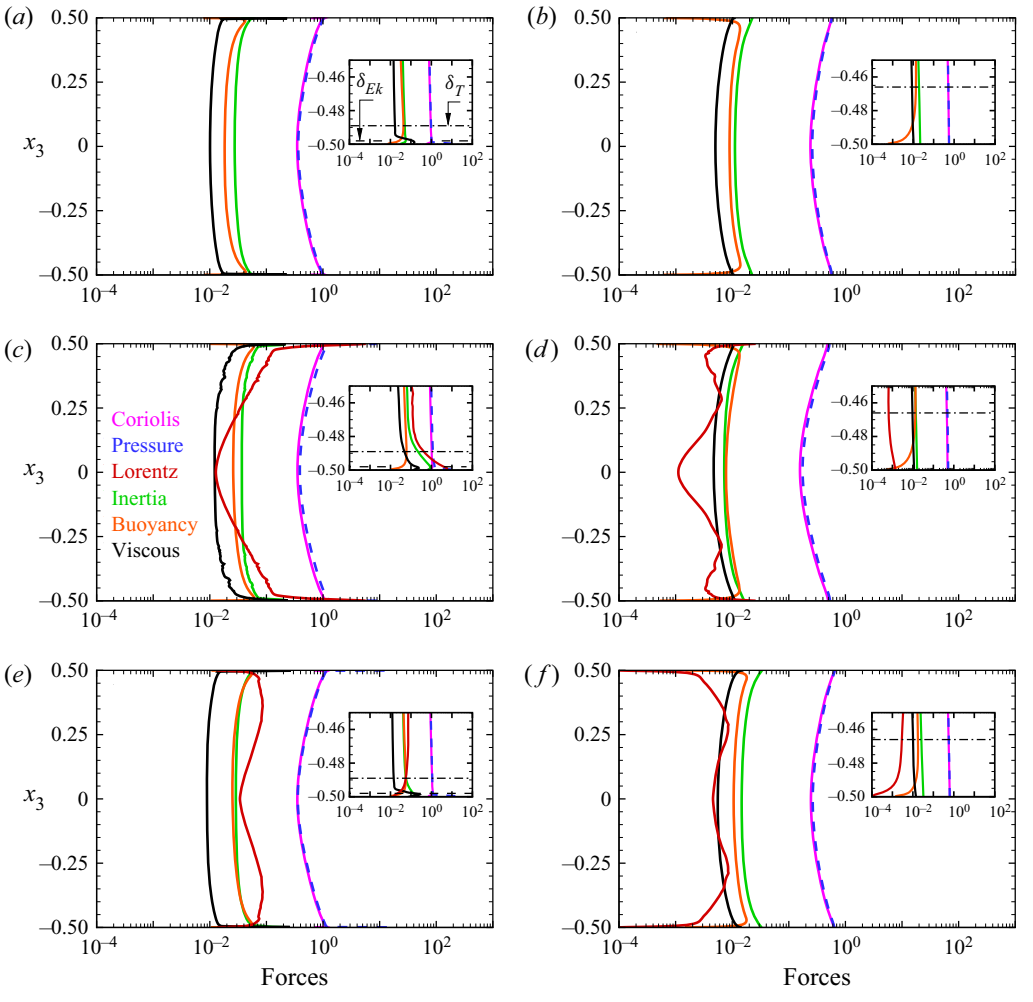

Figure 4. Vertical variation of forces for (*a*) NS, (*b*) FS, (*c*) NSC, (*d*) FSC, (*e*) NSV, (*f*) FSV cases at $\mathcal{R} = 3$. The horizontally averaged force distribution is shown in the bulk and near the bottom plate (inset).

$1/2\langle B_i B_i\rangle$ is the volume-averaged magnetic energy, and $B_\tau = \sqrt{\rho\mu}\, u_f (2M)^{1/2}$ is a characteristic value of the magnetic field. The magnetic field strength of the dynamos rises monotonically with increasing thermal forcing for all boundary conditions. However, the relative mean field strength $\bar{M}/M$, where $\bar{M} = 1/2\langle B_i\rangle\langle B_i\rangle$, is found to decrease (tables 1–4) with increasing $\mathcal{R}$, indicating a shift towards small-scale dynamo action with increasing thermal forcing (Tilgner 2012, 2014). We find 'energetically robust' dynamos at $\mathcal{R} = 2$ (corresponding to $\widetilde{Re}_m = Re_m\, Ek^{1/3} = O(1)$) with significant $\bar{M}/M$, confirming the findings of Yan & Calkins (2022*b*). The present study shows that such dynamos are generated for $\widetilde{Re}_m \approx O(1)$, irrespective of the boundary conditions.

3.2. *Force balance*

Now we look into the dynamical balances of the dynamos with different kinematic and magnetic boundary conditions at $\mathcal{R} = 3$. Figure 4 shows the vertical variation of the horizontally averaged forces, evaluated from the r.m.s. values of each term in the

momentum equation (2.2) (Guzmán *et al.* 2021; Yan *et al.* 2021). The figure presents the forces for no-slip (figures 4*a*,*c*,*e*) and free-slip (figures 4*b*,*d*,*f*) boundary conditions at $\mathcal{R} = 3$. Here, the RC simulation results (figures 4*a*,*b*) are used as a reference to interpret the results for DC simulations with perfectly conducting (figures 4*c*,*d*) and pseudo-vacuum (figures 4*e*,*f*) boundary conditions. At $\mathcal{R} = 3$, we get the thermal and Ekman boundary layer thickness as $\delta_T = 0.011$ and $\delta_{Ek} = 0.002$ for the no-slip cases, whereas the thermal layer thickness increases to $\delta_T = 0.034$ for the free-slip cases. The near-wall regions are magnified in the insets, with the velocity and thermal boundary layer edges marked by the black horizontal dashed and dash-dot lines, respectively, in figure 4(*a*). For all the cases shown in this plot, the leading-order balance between Coriolis and pressure force indicates a geostrophic state in the bulk. For non-magnetic rapid RC, geostrophic balance in the bulk has been confirmed by DNS (Guzmán *et al.* 2021), apart from reduced-order models in the rapidly rotating limit (Julien *et al.* 2012*b*). The DNS study of rapidly rotating DC by Yan & Calkins (2022*a*) has also found leading-order geostrophic balance, for FSV conditions. Departure from the geostrophic state due to the other forces, which constitute a lower-order quasi-geostrophic balance, makes turbulent convection possible. In the non-magnetic simulations (NS and FS) in figures 4(*a*) and 4(*b*), the geostrophic and quasi-geostrophic forces behave similarly except near the boundaries (see insets), where the viscous force break the geostrophic balance and dominate the other quasi-geostrophic forces (inertia and buoyancy) in the Ekman layer near the plates with the no-slip boundary condition.

For the dynamo simulations, the Lorentz force exerted by the magnetic field on the flow also enters the quasi-geostrophic balance. For the NSC case, as shown in figure 4(*c*), the Lorentz force is minimum at the mid-plane, which increases towards the walls to dominate the quasi-geostrophic balance for $x_3 \leqslant -0.25$. Inside the thermal boundary layer, the Lorentz force increases to the same order of magnitude as the Coriolis force, and eventually becomes the highest force at the wall. This is reflected by the value of the local Elsasser number Λ_T (the ratio of the r.m.s. magnitudes of the Lorentz and the Coriolis forces at the edge of the thermal boundary layer, calculated from the horizontally averaged variation of the two forces), as presented in tables 1–4. This increase in the Lorentz force at the thermal boundary layer edge leads to a local magnetorelaxation of the thermal boundary layer, which results in increased turbulence and heat transport (Naskar & Pal 2022). Similar behaviour of the Lorentz force near the boundary was found in the range $\mathcal{R} = 3$–5 for the NSC cases. However, no such enhancement of Lorentz force is found in the dynamo simulations with any other combinations of the boundary conditions. For the NSV case in figure 4(*e*), the Lorentz force is higher than the other quasi-geostrophic forces in the bulk, but decreases inside the thermal layer. Unlike the NSC case, the Lorentz force in the NSV case keeps decreasing towards the Ekman layer, where the viscous force dominates. The volume-averaged ratio of the Lorentz and Coriolis forces, Λ_V, is also presented in tables 1–4. This volume-averaged Elsasser number reaches a maximum near $\mathcal{R} = 4$ for the NSV case in table 2. The Lorentz force inside the thermal layer is one order of magnitude smaller than the other quasi-geostrophic forces for the FSC case in figure 4(*d*), making the near-wall balance similar to the non-magnetic RC (FS). Though the Lorentz force has magnitude similar to that of the viscous force in the bulk for the FSV cases in figure 4(*f*), it becomes the smallest force inside the thermal boundary layer, again making the balance similar to the FS case near the walls. Therefore, our results corroborate the finding of Yan & Calkins (2022*a*), that the Lorentz force acts as a small perturbation in the force balance, with magnitude similar to that of the viscous force, for the FSV boundaries. These results illustrate the dependence of the dynamical balance of the dynamo on the imposed

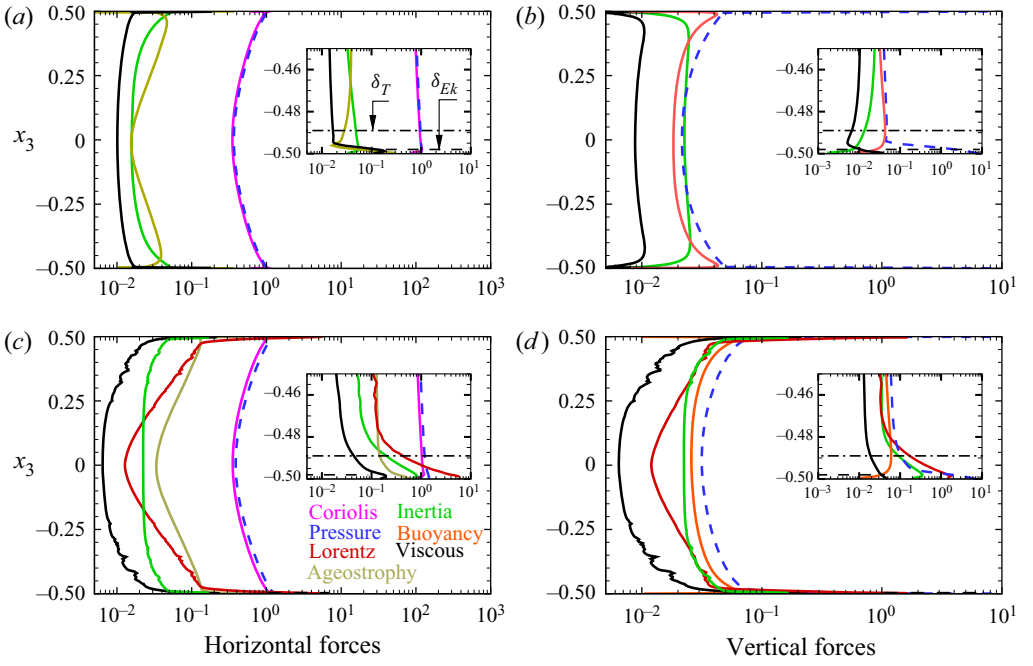

Figure 5. Vertical variation of the force components for (*a*,*b*) NS and (*c*,*d*) NSC cases. (*a*,*c*) Horizontal components of the forces $F_h = \sqrt{F_{x_1}^2 + F_{x_2}^2}$; (*b*,*d*) vertical components (F_{x_3}). The horizontally averaged force distribution is shown here at $\mathcal{R} = 3$ both in the bulk, and near the bottom plate (inset).

boundary conditions, especially near the boundary. Also, the dynamo simulations with no-slip conditions exhibit distinctive balance compared to the non-magnetic convection inside the thermal boundary layer. In contrast, the dynamical balance in the thermal layer is similar to RC for free-slip boundary conditions with negligible contribution from the Lorentz force. The magnetic boundary condition decide the magnitude and vertical distribution of the Lorentz force in the dynamos.

The force balance in the NSC case at $\mathcal{R} = 3$ exhibits some interesting features near the boundary layer, as shown in figure 4. This case can be analysed in more detail from figure 5, where the horizontal and vertical balances are illustrated separately and compared with the NS case. As the rotation axis is aligned with the vertical, the Coriolis force acts only in the horizontal planes, whereas the buoyancy force is purely vertical. In the non-magnetic NS case, the leading-order horizontal balance is geostrophic between the Coriolis and pressure forces, as depicted in figure 5(*a*). The ageostrophy, as defined by the difference between the two forces, is balanced by the inertia and viscous forces. Near the walls, there is a sharp increase in the ageostrophy, balanced by the viscous force, indicating a loss of geostrophic balance inside the viscous boundary layers, as seen in the inset of figure 5(*a*) (see also Guzmán *et al.* 2021). Among the vertical forces in figure 5(*b*), the vertical pressure gradient is balanced by the inertia and buoyancy forces in the bulk where the viscous forces remain small.

In the NSC case, the leading-order balance remains geostrophic in the horizontal direction, as presented in figure 5(*c*). However, the ageostrophy is much higher than the NS case due to magnetorelaxation of the Taylor–Proudman theorem in the presence of the Lorentz force. The ageostrophic component is balanced by the Lorentz and

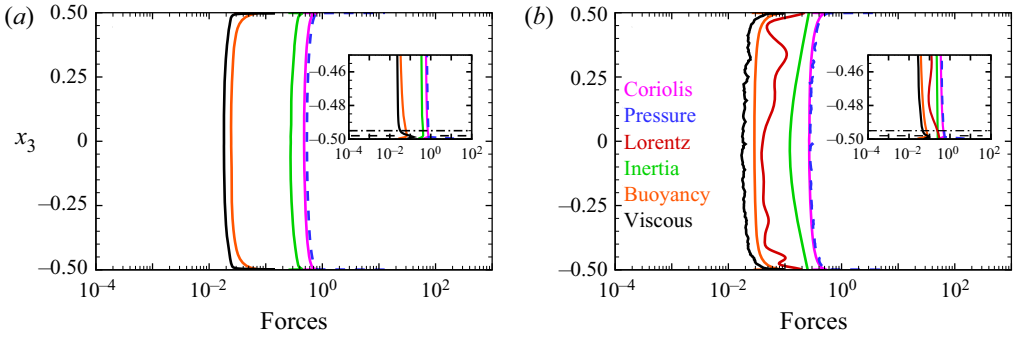

Figure 6. Vertical profiles of the forces for (*a*) NS, (*b*) NSC cases at $\mathcal{R} = 20$. The horizontally averaged force distribution is shown in the bulk and near the bottom plate (inset).

inertial forces in the bulk. In the vertical direction, the pressure force is balanced by the Lorentz, buoyancy and inertial forces, as shown in figure 5(*d*). We note here that the horizontal components of the forces are always higher than the vertical forces, with the force magnitudes enhanced near the boundaries for all the cases. The flow velocities gradually come to zero inside the Ekman layer, resulting in an increase in the pressure at the boundary. Furthermore, the details of the force balance, especially the role of inertia, depend on $\mathcal{R}$. With increase in $\mathcal{R}$, the inertial force eventually dominates the quasi-geostrophic balance, as observed for $\mathcal{R} = 20$ in figures 6(*a*) and 6(*b*) for the NS and NSC cases, respectively. This increase in inertia with thermal forcing corroborates the findings of Guzmán *et al.* (2021), and is a common feature among all boundary conditions. The local magnetorelaxation of the rotational constraint in the thermal boundary layer, as a mechanism for increase in heat transfer in the NSC case compared to the NS case, becomes gradually ineffective with increasing $\mathcal{R}$. This is because the increased inertia, rather than the Lorentz force, breaks the Taylor–Proudman constraint for both RC and DC simulations, irrespective of boundary conditions.

3.3. *Energy budget*

We further analyse the various energetic terms in the TKE budget equation (A1) to illustrate the generation of TKE from thermal forcing, and its dissipation and conversion to magnetic energy for elucidating the turbulent dynamo mechanism. The significance of the TKE budget terms and their dependence on the boundary conditions have been explored, with particular attention paid to the near-wall features. In figure 7, the various terms in the TKE budget equation (see Appendix A) are plotted with the near-wall variation shown in the inset. All the terms are averaged in the horizontal planes, and their variation in the vertical direction is shown at $\mathcal{R} = 3$ with varying boundary conditions. For the NS and FS cases, in figures 7(*a*) and 7(*b*), the primary energy balance is between the buoyant production ($\mathcal{B}$) and viscous dissipation (ϵ_v). The transport term $\partial \mathcal{T}_j/\partial x_j$ acts to redistribute the energy and becomes zero when averaged over the volume. This term includes the combined effect of diffusive transport, pressure transport and third-order correlation terms (see (A3)). A detailed discussion of a typical energy budget in RC with the individual treatment of these terms can be found in Kunnen, Geurts & Clercx (2009). In the absence of a mean flow, the shear production term P is zero, whereas the unsteady term $\partial K/\partial t$ also becomes zero in the statistically stationary state. In the bulk, for the

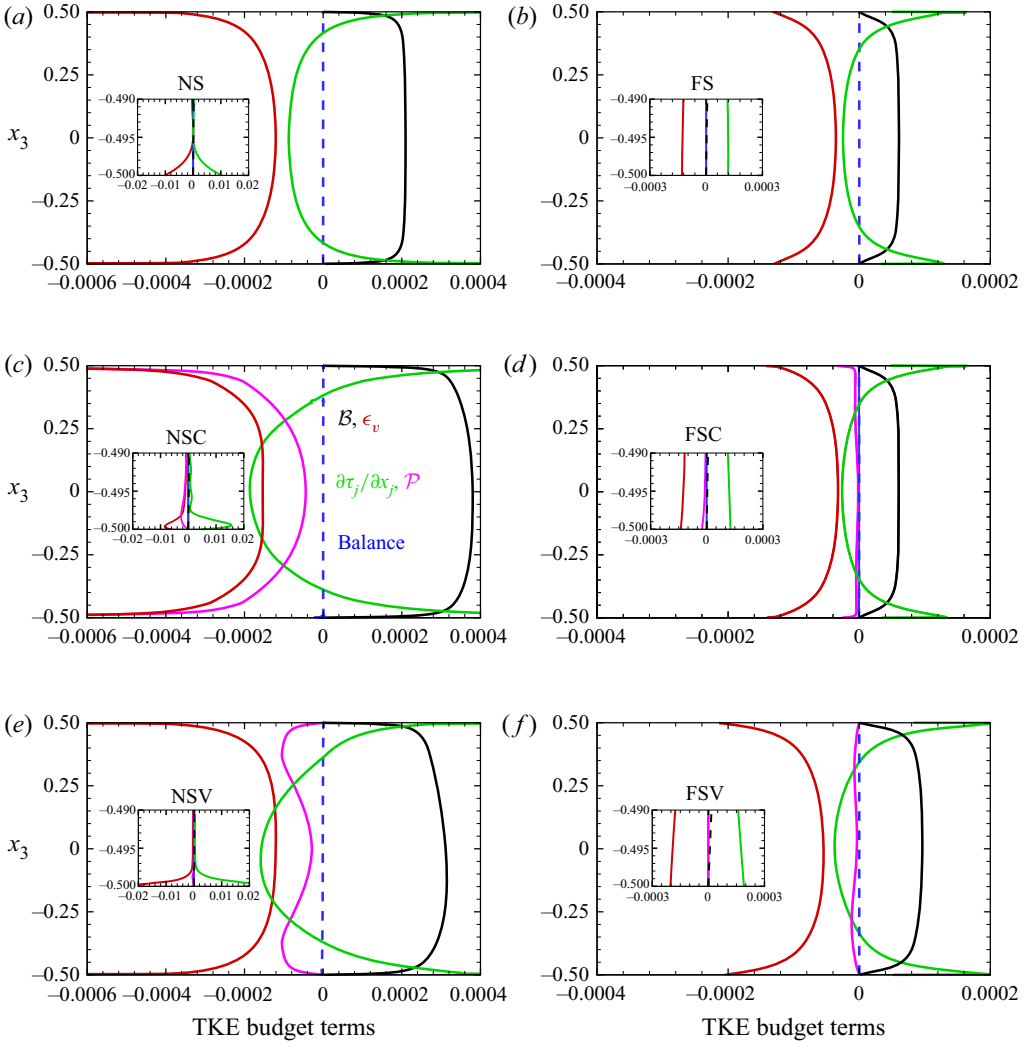

Figure 7. Vertical variation of TKE budget terms at $\mathcal{R} = 3$ for both no-slip (*a*,*c*,*e*) and free-slip (*b*,*d*,*f*) boundaries. Energy budget terms are presented for non-magnetic simulations (*a*,*b*) as well as dynamo simulations with both perfectly conducting (*c*,*d*) and pseudo-vacuum (*e*,*f*) conditions. The horizontally averaged budget terms in (A1) are averaged in time. The profiles near the bottom wall are magnified in the insets. The balance terms signify the difference between the left- and right-hand sides of (A1), and indicate sufficient accuracy of the present calculations.

non-magnetic RC cases (as shown in figures 7*a*,*b*), some part of the TKE generated from the buoyant production is converted to thermal energy by viscous dissipation, and the rest is redistributed by the transport term. Near the boundaries, this transport of kinetic energy term transfers energy from the bulk towards the boundary layers, which undergoes viscous dissipation. Hence the primary balance is between the dissipation and transport terms near the plates. Due to the presence of viscous Ekman layers in the NS case, the viscous dissipation (and therefore the kinetic energy transport) increases by two orders of magnitude near the plates compared to their bulk values, as shown in the inset of figure 7(*a*). Such an order of magnitude jump is not present for the FS case in figure 7(*b*) owing to the absence of the Ekman boundary layer.

For the dynamos, the magnetic production of TKE ($\mathcal{P}$) appears in (A1) to represent the work done by the Lorentz force on the velocity field to produce TKE. A negative value of this term indicates transfer of energy from the velocity field to the magnetic field, and vice versa. This term is responsible for converting some part of the kinetic energy to magnetic energy to sustain dynamo action. For all the dynamo cases (NSC, NSV, FSC and FSV), $\mathcal{P}$ appears as an additional sink of TKE that balances the buoyant production of kinetic energy together with viscous dissipation. The behaviour of magnetic production is similar to viscous dissipation for the NSC case. Here, the budget terms show a peak near the edge of the Ekman layer, as shown in the inset of figure 7(*c*). For the NSV boundary condition in figure 7(*e*), the magnetic production term is not significant near the mid-plane but increases towards the boundary to reach a peak near $x = \pm 0.4$ before it decreases to zero at the wall. For FSC and FSV conditions, the contribution from this term is not significant to the overall budget, as plotted in figures 7(*d*) and 7(*f*). This magnetic production term in the TKE budget comprises of three components, $\mathcal{P}_1$, $\mathcal{P}_2$ and $\mathcal{P}_3$, as expressed in (A4*a–c*). Out of these, the first two magnetic production terms involving the mean magnetic field and its gradients ($\mathcal{P}_1$ and $\mathcal{P}_2$) are found to be small compared to $\mathcal{P}_3$ at $\mathcal{R} = 3$. It should be noted here that for lower convective supercriticality, the mean magnetic field may become strong compared to the turbulent magnetic field, and therefore the terms $\mathcal{P}_1$ and $\mathcal{P}_2$ may contribute significantly to magnetic production. The transport of kinetic energy by the mean and fluctuating magnetic fields, as represented by the last two terms in the right-hand side of (A3), are also found to be small compared to the pressure transport and turbulent transport terms (figure not presented).

The dominant term among the magnetic production terms, $\mathcal{P}_3$, represents the work done by the fluctuating magnetic field on the fluctuating velocity field to produce TKE. It is interesting to study this term for elucidating the mechanism of energy exchange between these two vector fields. The nine components of this term are represented by $\mathcal{P}_3^{ij} = \overline{B_i' B_j' \, \partial u_i'/\partial x_j}$ in figure 8 for the NSC and NSV cases where magnetic production makes a significant contribution to the TKE budget. Among these nine components, the three terms involving the vertical gradient of the fluctuating velocity field, $\mathcal{P}_3^{i3} = \overline{B_i' B_3' \, \partial u_i'/\partial x_3}$ (where $i = 1, 2, 3$) are small due to the Taylor–Proudman constraint on the velocity field imposed by rotation that suppresses changes in the vertical direction. Interestingly, for the NSC case, there are components with both positive and negative values in figure 8(*a*). Here, the components $\mathcal{P}_3^{11}$ and $\mathcal{P}_3^{21}$ become positive away from the mid-plane, indicating a transfer of energy from the magnetic field to the velocity field. Vertical variations of the terms $\mathcal{P}_3^{12}$ and $\mathcal{P}_3^{22}$ are similar but opposite, with negative values away from the mid-plane indicating transfer of energy from the velocity to the magnetic field. The last two negative terms, being larger than the positive terms, provide a bias in the direction of energy transfer so that the system can extract kinetic energy of the fluid and convert it to magnetic energy to sustain dynamo action. However, at the mid-plane, all the terms are negative. Near the wall, these four terms exhibit peaks near the edge of the Ekman boundary layer where the values are two orders of magnitude higher than at the mid-plane. The two remaining terms, $\mathcal{P}_3^{31}$ and $\mathcal{P}_3^{32}$, are small compared to the dominant terms near the wall, but contribute most to the energy transfer at the mid-plane. In the NSV case, all the components of work done by the Lorentz force $\mathcal{P}_3^{ij}$ are negative, indicating unidirectional energy transfer from the velocity field to the magnetic field. This demonstrates that the imposed boundary conditions dictate the energy

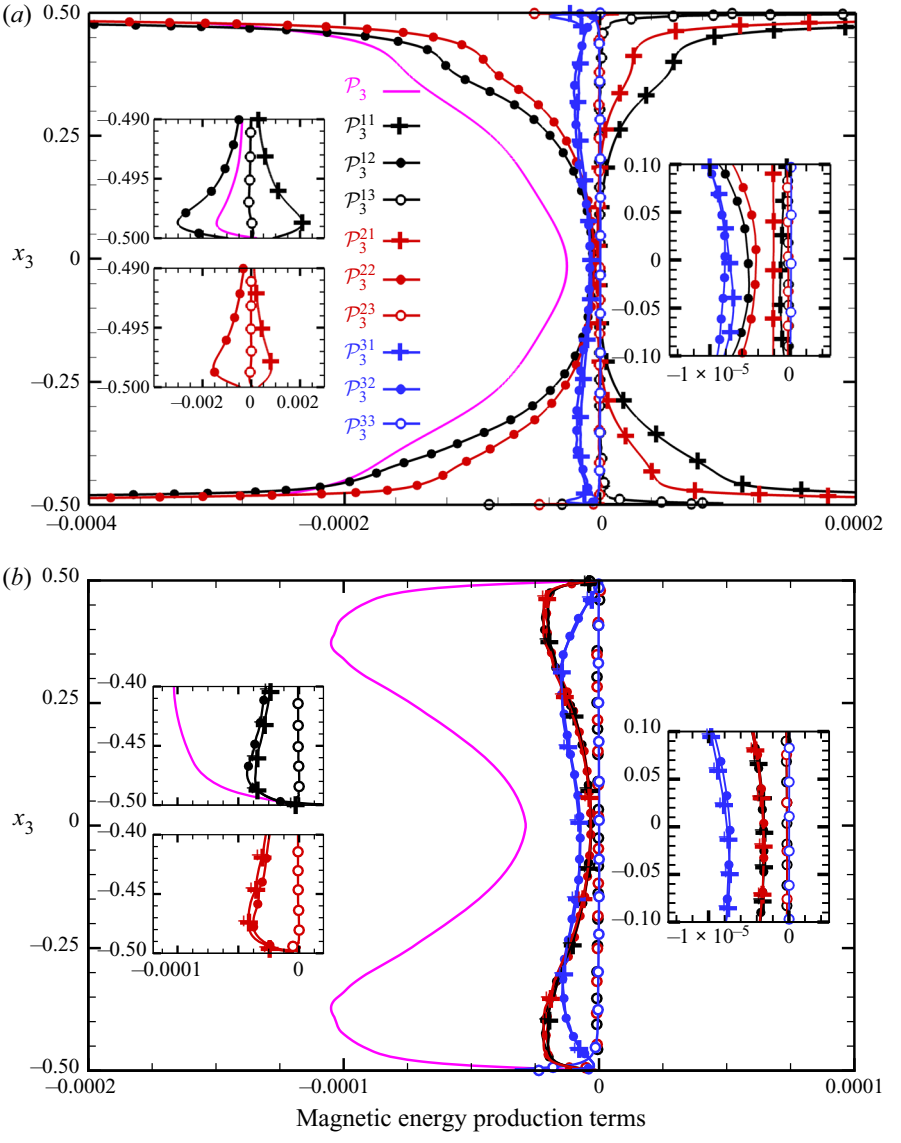

Figure 8. Variation of the magnetic production terms for (*a*) NSC and (*b*) NSV cases at $\mathcal{R} = 3$. The components of the work done by the Lorentz force $\mathcal{P}_3$ are represented by the colours: black for $i = 1$, red for $i = 2$, and blue for $i = 3$. Here, the lines with + symbols and filled and open circles represent $j = 1$, $j = 2$ and $j = 3$, respectively.

exchange mechanism between the velocity and magnetic fields, both in the bulk and near the boundaries.

The volume-averaged budget of turbulent magnetic energy, reduces to a balance between the magnetic energy production and the Joule dissipation, $\langle \mathcal{P} \rangle = \langle \epsilon_j \rangle$, for statistically stationary turbulence. This signifies that the part of TKE converted to magnetic energy ultimately converts to thermal energy via Joule dissipation. The Ohmic fraction, defined by the ratio of Joule dissipation to total dissipation $\langle \epsilon_j \rangle / \langle \epsilon \rangle$, is presented in tables 1–4. The Ohmic fraction does not show any particular trend in the range $\mathcal{R} = 2$–20. The global

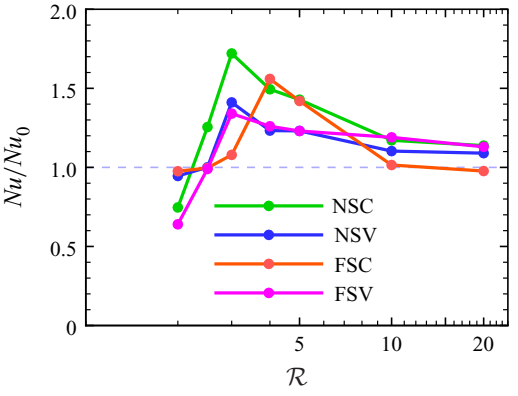

Figure 9. Variation of the Nusselt number ratio Nu/Nu_0 as a function of the thermal forcing for different boundary conditions. Here, Nu_0 represents the Nusselt number for the non-magnetic RC simulations.

energy balance between buoyant production $\langle \mathcal{B} \rangle$ and total dissipation $\langle \epsilon \rangle$ is also presented in these tables, where the values have been scaled by a factor 10^4. The difference between the two terms never exceeds 5 % of $\langle \mathcal{B} \rangle$, indicating the accuracy of the present DNS in capturing all the energy-containing scales. The vertical trends of the terms in the TKE equation remain similar to those presented in figure 7 over the range of thermal forcing studied here. The volume-averaged buoyancy flux and dissipation increase by an order of magnitude in the range $\mathcal{R} = 2$–20.

3.4. *Heat transfer behaviour*

Finally, we study the heat transfer behaviour of the dynamo simulations with increasing thermal forcing under the influence of different boundary conditions. In figure 9, the Nusselt number ratio Nu/Nu_0 signifies the change in heat transport in DC simulations due to dynamo action compared to the non-magnetic RC simulations. For NSC, a peak is found near $\mathcal{R} = 3$, with more than 72 % enhancement in heat transfer. A peak in Nusselt number ratio is also found for the NSV case at $\mathcal{R} = 3$, with a 41 % increase in heat transport compared to non-magnetic RC. For FSC and FSV cases, the heat transfer ratio also peaks at $\mathcal{R} = 4$ and $\mathcal{R} = 3$, with enhancement up to 56 % and 34 %, respectively. The ratio of viscous dissipation in the DC and RC simulations $\langle \epsilon_v \rangle / \langle \epsilon_0 \rangle$ is also presented in tables 1–4, which shows a similar trend with the Nusselt number ratio. The peaks in heat transfer ratio and the viscous dissipation ratio occur at the same value of $\mathcal{R}$. We note here that the overall energy balance of the system leads to an exact relation between the Nusselt number and the total dissipation, $Nu = 1 + \sqrt{Ra\,Pr}\,\langle \epsilon \rangle$. Hence the dissipation ratio should behave similarly to the Nusselt number ratio with varying $\mathcal{R}$, as seen in tables 1–4. A local magnetorelaxation of the rotational constraint, due to enhanced Lorentz force in the thermal boundary layer (see figure 4*c*), has been proposed to be the reason for the rise in heat transfer in the NSC case (Naskar & Pal 2022). However, the build-up of the Lorentz force required for this magnetorelaxation process is not present for any other combinations of the boundary conditions (see figure 4). Notably, in the NSV case, the Lorentz force in the bulk is higher compared to the other cases in figure 4(*e*). Indeed, the volume-averaged Elsasser number Λ_V in table 2 shows a peak at $\mathcal{R} = 3$ that correlates well with the heat transfer behaviour. Therefore, the global relaxation of the Taylor–Proudman constraint is a possible mechanism for the heat transfer enhancement. For the free-slip cases, the heat

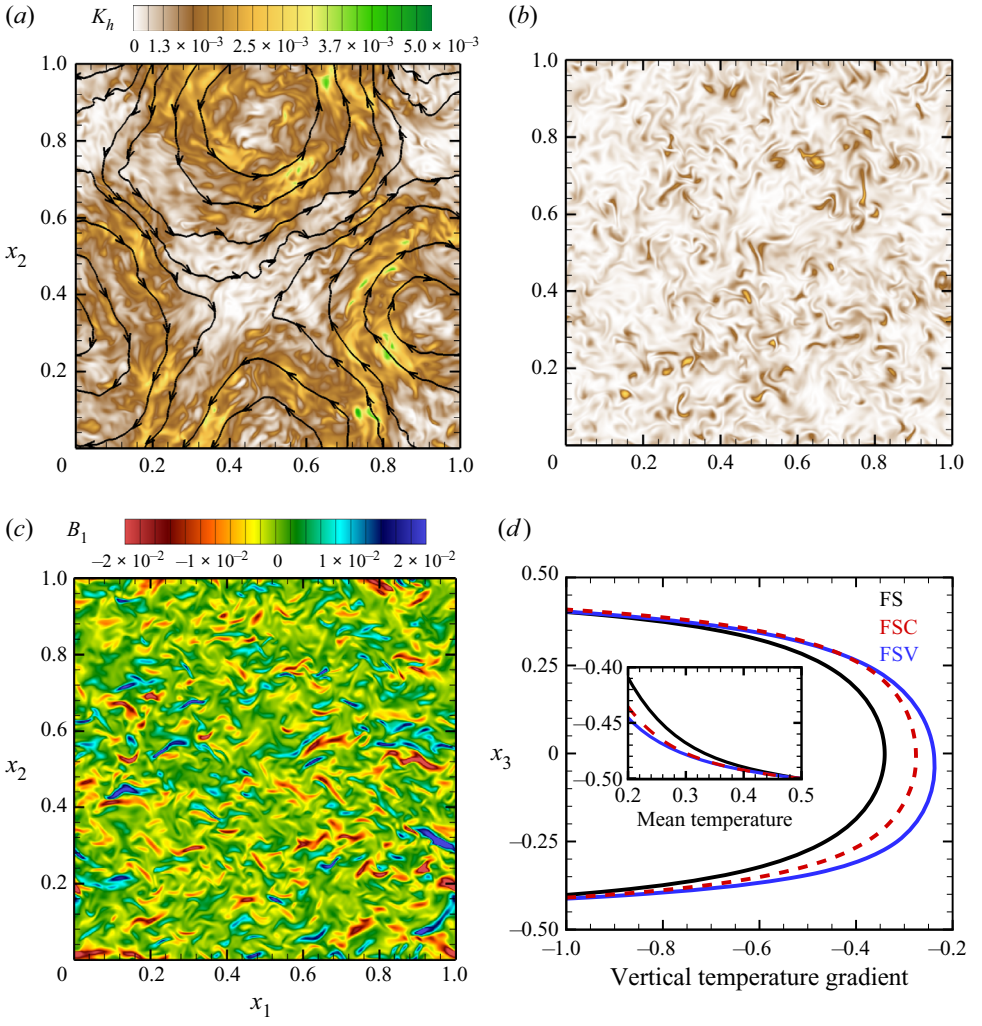

Figure 10. Contours of horizontal TKE, $K_h = 1/2(u_1^2 + u_2^2)$ for (*a*) FS and (*b*) FSC cases at $\mathcal{R} = 4$. The instantaneous plots are shown in the horizontal mid-plane at $x_3 = 0.5$ to illustrate the presence of LSV in (*a*), which is superimposed with streamlines. The dynamo simulation with FSC conditions generates small-scale velocity and magnetic fields as illustrated by contours of TKE and magnetic field B_1 in (*b*,*c*), respectively. The vertical temperature gradients at $\mathcal{R} = 4$ are shown in (*d*) for the free-slip cases. The mean temperature profile near the lower wall is also shown in the inset.

transfer enhancement in dynamos is achieved by suppression of LSV by the small-scale magnetic field, as discussed in the next paragraph. It is interesting to note that the peak in heat transfer ratio appears within a narrow range of thermal forcing $\mathcal{R} = 3$–4, depending on the conditions at the boundary. Further investigations will be necessary to elucidate the appearance of the peak in heat transfer ratio for different boundary conditions. However, the heat transport properties of the dynamo depend on the boundary conditions and the associated dynamical balances both in the bulk and in the boundary layer.

The heat transfer enhancement in the dynamos with free-slip boundary conditions with respect to non-magnetic RC can be attributed to the absence of LSV in the former. In the FS cases, we find the presence of depth-independent, long-lived (compared to the free-fall

time scale) LSV for $\mathcal{R} \geqslant 4$, corroborating the findings of Guervilly *et al.* (2014). Similar to freely decaying two-dimensional turbulence, the formation of LSV in RC involves an upscale energy transfer from the convective eddies to large-scale barotropic modes (Favier, Silvers & Proctor 2014; Rubio *et al.* 2014). The flow associated with these structures is nearly two-dimensional, which can be visualized from the contours of horizontal TKE, $K_h = 1/2(u_1^2 + u_2^2)$, which tends to be high in the shear layer around the core of these vortices, as shown in figure 10(*a*) for $\mathcal{R} = 4$. An animation of the LSV, as visualized by the time evolution of the K_h contours, can be found in the supplementary movie available at https://doi.org/10.1017/jfm.2022.841. Here, we find a pair of cyclonic and anti-cyclonic vortices centred around $(0.48, 0.87)$ and $(0.93, 0.34)$, respectively, as depicted in the horizontal mid-plane at $x_3 = 0.5$. The degree to which the two-dimensionality of the flow has been induced by the presence of an LSV can be measured by the ratio $\tau = \langle u_1^2 + u_2^2 + u_3^2 \rangle / 3\langle u_3^2 \rangle$, as reported in tables 1–4. The kinetic energy ratio for the RC simulations τ_0 is also reported in tables 2 and 3 for the NS and FS cases, respectively. As the kinetic energy associated with the horizontal flow in the LSV is higher than the kinetic energy in the vertical flow, the value of τ increases to values much higher than unity in the FS cases for $\mathcal{R} \geqslant 4$. We have also found LSV with no-slip boundary conditions without magnetic field (NS case) for $\mathcal{R} = 10$ and 20, which supports the findings of Guzmán *et al.* (2020) that LSV appear in RC irrespective of the kinematic boundary condition. However, the presence of no-slip boundaries suppresses the formation of LSV until higher convective supercriticality ($\mathcal{R} \geqslant 10$) compared to the free-slip cases ($\mathcal{R} \geqslant 4$).

Guervilly *et al.* (2017) reported that for $Re_m \geqslant 550$, the formation of LSV can be suppressed by the presence of a small-scale magnetic field. Such a field acts to disrupt the correlations between the convective vortices that in turn hinder the upscale transfer of energy. This should be the reason why we do not find any LSV in our dynamo simulations with free-slip conditions that operate for $Re_m \geqslant 641$. The combined effect of the no-slip boundary condition and the presence of a magnetic field has suppressed the LSV in the NSC and NSV cases as well, as reflected by the value of τ in tables 1 and 2. Maffei *et al.* (2019) used an asymptotic magnetohydrodynamic model to study the effect of an imposed magnetic field on the inverse cascade of energy in the turbulent geostrophic regime of RC. The possibility of occurrence of LSV in the presence of the magnetic field was quantified by an interaction parameter N, which signifies the relative strengths of the Lorentz force and the non-linear advection. For $N \geqslant 0.013$, the magnetic field disrupts the upscale energy transfer, hence LSV can be present only below this limit. We have calculated the interaction parameter as a ratio of the volume-averaged r.m.s. magnitudes of the Lorentz force and the nonlinear advection terms, and found the ratio to be of $O(10^{-1})$ for all our dynamo simulations. Though the self-excited magnetic fields in our dynamo simulations are not directly comparable to the externally imposed field used by Maffei *et al.* (2019), the magnetic quenching of the inverse cascade is a plausible mechanism for the disappearance of LSV in our dynamo simulations. The horizontal TKE and the x_1 component of the magnetic field for FSC cases, as depicted in figures 10(*b*) and 10(*c*), show small-scale fields without any trace of LSV. The presence of LSV can disrupt the vertical mixing by transferring energy to horizontal barotropic modes (Guervilly *et al.* 2014). In figure 10(*d*), this phenomenon results in an increased gradient of temperature in the bulk for the FS case with LSV, compared to the FSC and FSV cases without LSV. The temperature profiles near the wall (see inset) show higher thermal boundary layer thickness in the FS case compared to the dynamo cases, indicating a decrease in heat transfer efficiency near the wall in the FS case. The thermal plumes near the wall get

swept away by the horizontal flow associated with LSV, which can interrupt the vertical transport of heat by the plumes, leading to a decrease in the heat transfer efficiency.

4. Conclusions

We have performed high-fidelity DNS of dynamos driven by rapidly rotating RBC under four combinations of kinematic and magnetic boundary conditions. The simulations are performed in the rotation-dominated regime $\mathcal{R} = 2$–20 at a fixed rotation rate $Ek = 5 \times 10^{-7}$ and fluid properties $Pr = Pr_m = 1$. The dynamo simulations with the no-slip and free-slip kinematic boundary conditions combined with the perfectly conducting and pseudo-vacuum magnetic boundary conditions (NSC, NSV, FSC and FSV) are compared against non-magnetic simulations (NS and FS) to study the impact of the dynamo action on the convective flow properties. Our previous study (Naskar & Pal 2022) reported the existence of optimal heat transfer enhancement with respect to non-magnetic convection due to dynamo action for NSC boundary conditions at $\mathcal{R} = 3$. Therefore, we have chosen this case to compare the statistics of the velocity, thermal and magnetic fields in addition to the dynamical balance, energy budget and heat transfer behaviour of the dynamos.

The flow and thermal field of the dynamos, apart from the structure of the magnetic field, are found to depend on the boundary conditions. Ekman pumping significantly enhances the velocity and thermal fluctuations in the dynamos, increasing the r.m.s. velocities and temperatures both in the bulk and near the boundaries. It also leads to a three orders of magnitude increase in enstrophy, signifying increased strength of the vortical plumes inside the Ekman layer with the no-slip boundary condition. The relative helicity also exhibits a peak near the Ekman layer, illustrating strong correlations between the velocity and vorticity fields. The perfectly conducting boundary conditions can trap the magnetic field near the boundaries to prevent its escape and make it purely horizontal. This leads to a jump of r.m.s. horizontal field strength near the boundaries for the NSC case. The r.m.s. field strength remains higher than the mean field for all combinations of the boundary conditions in the investigated range of thermal forcing.

The leading-order force balance in the dynamos remains geostrophic, similar to our non-magnetic RC simulations, irrespective of the boundary conditions. At $\mathcal{R} = 3$, the quasi-geostrophic balance corresponds to a Coriolis-inertial-Archimedean force balance between the ageostrophic part of Coriolis, inertia and buoyancy forces in the non-magnetic simulations. The extent to which the Lorentz force modulates the quasi-geostrophic balance is decided by the boundary conditions in the dynamo simulations. For NSC conditions, a build-up of the Lorentz force is seen near the walls, whereas this force dominates the quasi-geostrophic balance in the bulk for NSV conditions. For free-slip conditions, the Lorentz force is much weaker compared to the no-slip dynamos.

The budget of TKE for the non-magnetic cases exhibits an overall balance between the buoyant production and viscous dissipation. For the NS case, the viscous dissipation increases by two orders of magnitude from its bulk value due to viscous action inside the Ekman layer. For the dynamo simulations, some part of the TKE is converted to magnetic energy via work done by the Lorentz force, which is ultimately converted to thermal energy by the Joule dissipation. This additional term, signifying the production of magnetic energy in the dynamo simulations, is considerably weaker with free-slip boundaries than no-slip boundaries. A break up of the components that constitute this production of magnetic energy term (which can also be interpreted as the work done by the Lorentz force on the flow) reveals that the energy flows both ways, from the velocity field

to the magnetic field and vice versa, when NSC conditions are imposed at the boundary. Conversely, the flow of energy is unidirectional, from kinetic energy to magnetic energy, when the NSV boundary condition is used, indicating the decisive role of the boundary conditions on the mechanism of energy transfer.

Another interesting finding of our study is the enhancement of heat transfer in the DC simulations with respect to the non-magnetic RC simulations. The heat transfer enhancement reaches a peak in the range $\mathcal{R} = 3$–4 for all the combinations of boundary conditions. The magnetorelaxation of the rotational constraint by the Lorentz force is the mechanism for heat transfer enhancement for the no-slip cases, whereas for the free-slip dynamos, the suppression of LSV by magnetic field is found to be the reason behind the increased efficiency of heat transport. We have found the LSV in our non-magnetic simulations that are known to deteriorate the heat transfer, as reported in the literature (Guervilly *et al.* 2014). By comparing our results with the existing literature, we conclude that the magnetic quenching of LSV by the magnetic field is a possible reason for the heat transfer enhancement in our free-slip dynamo simulations. An interesting extension of the present study will be the search for power-law scaling of the heat transfer and flow speed with the thermal forcing in such convection-driven dynamos, and the effect of boundary conditions on the power-law exponent and the prefactor.

Finally, we would like to point out that the near-wall force balance and the heat transfer behaviour of rotating DC should also depend on Pr, along with the boundary conditions. The length scale at which the Lorentz force enters the force balance (Aurnou & King 2017; Schwaiger, Gastine & Aubert 2019), apart from its dependence on Pr_m (if any), also warrants future investigations.

Supplementary movie. A supplementary movie depicting large-scale vortices is available at https://doi.org/10.1017/jfm.2022.841.

Funding. We gratefully acknowledge the support of the Science and Engineering Research Board, Government of India grant no. SERB/ME/2020318. We also want to thank the Office of Research and Development, Indian Institute of Technology, Kanpur for financial support through grant no. IITK/ME/2019194. The support and the resources provided by PARAM Sanganak under the National Supercomputing Mission, Government of India at the Indian Institute of Technology, Kanpur are gratefully acknowledged.

Declaration of interests. The authors report no conflict of interest.

Author ORCIDs.
Souvik Naskar https://orcid.org/0000-0003-0445-8417;
Anikesh Pal https://orcid.org/0000-0003-2085-7231.

Author contributions. The authors contributed equally to analysing data and reaching conclusions, and in writing the paper.

Appendix A

The TKE equation for a rapidly rotating dynamo can be derived by including the terms involving work done by the Lorentz force. We note here that the Coriolis force is a pseudo-force and does not enter the balance directly. The evolution of the horizontally averaged TKE (see § 3.1 for the definition of the averages) can be written as

$$\frac{\mathrm{d}K}{\mathrm{d}t} = -P + \mathcal{B} - \epsilon_v - \frac{\partial \mathcal{T}_j}{\partial x_j} + \mathcal{P}, \tag{A1}$$

where

$$K = \frac{1}{2}\overline{u_i' u_i'}, \quad P = -\overline{u_i' u_j'}\,\frac{\partial \overline{u_i}}{\partial x_j}, \quad \mathcal{B} = \overline{u_3' \theta'}, \quad \epsilon_v = \sqrt{\frac{Pr}{Ra}}\,\overline{\frac{\partial u_i'}{\partial x_j}\,\frac{\partial u_i'}{\partial x_j}} \tag{A2a–d}$$

are the TKE, shear production, buoyancy flux and viscous dissipation. The transport of K is

$$\mathcal{T}_j = \overline{u_j' p'} + \frac{1}{2}\overline{u_i' u_i' u_j'} - \sqrt{\frac{Pr}{Ra}}\,\frac{\partial^2 K}{\partial x_j\,\partial x_j} - \overline{B_j}\,\overline{u_i' B_i'} - \overline{u_i' B_i' B_j'}. \tag{A3}$$

The shear production term P in (A2*b*) is negligible in the absence of a mean flow in the present simulations. However, shear production may still arise in the presence of a mean vertical motion through the turbulent transport term in (A3) (Kerr 2001). The last term on the right-hand side of (A1) is the production of K due to the work done by the Lorentz force on the flow field:

$$\mathcal{P}_1 = -\overline{B_j}\,\overline{B_i'\,\frac{\partial u_i'}{\partial x_j}}, \quad \mathcal{P}_2 = \overline{u_i' B_j'}\,\frac{\partial \overline{B_i}}{\partial x_j}, \quad \mathcal{P}_3 = -\overline{B_i' B_j'\,\frac{\partial u_i'}{\partial x_j}}, \quad \mathcal{P} = \mathcal{P}_1 + \mathcal{P}_2 + \mathcal{P}_3. \tag{A4a–d}$$

These magnetic production terms $\mathcal{P}_1$ to $\mathcal{P}_3$ in (A4*a–c*) represent the exchange of energy between the velocity and the magnetic fields. For example, $\mathcal{P}_1$ signifies the production of TKE due to work done by the mean magnetic field on the fluctuating strain rate of the velocity field. Furthermore, $\mathcal{P}_2$ represents the production of TKE due to the mean magnetic field gradient, analogous to the shear production term P in (A2*b*). The amplification (or attenuation) of the magnetic energy, due to the work done by stretching (or squeezing) of magnetic field lines by the fluctuating velocity gradients, is represented by the term $\mathcal{P}_3$. The terms $\mathcal{P}_1$ and $\mathcal{P}_2$, apart from the last two terms in (A3), representing the transport of kinetic energy by the magnetic field, remain small except at $\mathcal{R} = 2$.

References

Aurnou, J.M., Bertin, V., Grannan, A.M., Horn, S. & Vogt, T. 2018 Rotating thermal convection in liquid gallium: multi-modal flow, absent steady columns. *J. Fluid Mech.* **846**, 846–876.

Aurnou, J.M., Horn, S. & Julien, K. 2020 Connections between nonrotating, slowly rotating, and rapidly rotating turbulent convection transport scalings. *Phys. Rev. Res.* **2** (4), 043115.

Aurnou, J.M. & King, E.M. 2017 The cross-over to magnetostrophic convection in planetary dynamo systems. *Proc. R. Soc. Lond.* A **473** (2199), 20160731.

Brucker, K.A. & Sarkar, S. 2010 A comparative study of self-propelled and towed wakes in a stratified fluid. *J. Fluid Mech.* **652**, 373–404.

Calkins, M.A. 2018 Quasi-geostrophic dynamo theory. *Phys. Earth Planet. Inter.* **276**, 182–189.

Calkins, M.A., Julien, K., Tobias, S.M. & Aurnou, J.M. 2015 A multiscale dynamo model driven by quasi-geostrophic convection. *J. Fluid Mech.* **780**, 143–166.

Cattaneo, F. & Hughes, D.W. 2006 Dynamo action in a rotating convective layer. *J. Fluid Mech.* **553**, 401–418.

Chandrasekhar, S. 1961 *Hydrodynamic and Hydromagnetic Stability*. Courier Corporation.

Cheng, J.S., Madonia, M., Guzmán, A.J.A. & Kunnen, R.P.J. 2020 Laboratory exploration of heat transfer regimes in rapidly rotating turbulent convection. *Phys. Rev. Fluids* **5** (11), 113501.

Cheng, J.S., Stellmach, S., Ribeiro, A., Grannan, A., King, E.M. & Aurnou, J.M. 2015 Laboratory-numerical models of rapidly rotating convection in planetary cores. *Geophys. J. Intl* **201** (1), 1–17.

Childress, S. & Soward, A.M. 1972 Convection-driven hydromagnetic dynamo. *Phys. Rev. Lett.* **29** (13), 837.

CNOSSEN, I. 2014 The importance of geomagnetic field changes versus rising CO_2 levels for long-term change in the upper atmosphere. *J. Space Weather Space Clim.* **4**, A18.

ECKE, R.E. & NIEMELA, J.J. 2014 Heat transport in the geostrophic regime of rotating Rayleigh–Bénard convection. *Phys. Rev. Lett.* **113** (11), 114301.

ERDMANN, W., KMITA, H., KOSICKI, J.Z. & KACZMAREK, Ł. 2021 How the geomagnetic field influences life on Earth – an integrated approach to geomagnetobiology. *Orig. Life Evol. Biosph.* **51**, 231–257.

FAUTRELLE, Y. & CHILDRESS, S. 1982 Convective dynamos with intermediate and strong fields. *Geophys. Astrophys. Fluid Dyn.* **22** (3–4), 235–279.

FAVIER, B., SILVERS, L.J. & PROCTOR, M.R.E. 2014 Inverse cascade and symmetry breaking in rapidly rotating Boussinesq convection. *Phys. Fluids* **26** (9), 096605.

GUERVILLY, C., HUGHES, D.W. & JONES, C.A. 2014 Large-scale vortices in rapidly rotating Rayleigh–Bénard convection. *J. Fluid Mech.* **758**, 407–435.

GUERVILLY, C., HUGHES, D.W. & JONES, C.A. 2015 Generation of magnetic fields by large-scale vortices in rotating convection. *Phys. Rev.* E **91** (4), 041001.

GUERVILLY, C., HUGHES, D.W. & JONES, C.A. 2017 Large-scale-vortex dynamos in planar rotating convection. *J. Fluid Mech.* **815**, 333–360.

GUZMÁN, A.J.A., MADONIA, M., CHENG, J.S., OSTILLA-MÓNICO, R., CLERCX, H.J.H. & KUNNEN, R.P.J. 2020 Competition between Ekman plumes and vortex condensates in rapidly rotating thermal convection. *Phys. Rev. Lett.* **125** (21), 214501.

GUZMÁN, A.J.A., MADONIA, M., CHENG, J.S., OSTILLA-MÓNICO, R., CLERCX, H.J.H. & KUNNEN, R.P.J. 2021 Force balance in rapidly rotating Rayleigh–Bénard convection. *J. Fluid Mech.* **928**, A16.

IYER, K.P., SCHEEL, J.D., SCHUMACHER, J. & SREENIVASAN, K.R. 2020 Classical 1/3 scaling of convection holds up to $Ra = 10^{15}$. *Proc. Natl Acad. Sci. USA* **117** (14), 7594–7598.

JONES, C.A. & ROBERTS, P.H. 2000 Convection-driven dynamos in a rotating plane layer. *J. Fluid Mech.* **404**, 311–343.

JULIEN, K., AURNOU, J.M., CALKINS, M.A., KNOBLOCH, E., MARTI, P., STELLMACH, S. & VASIL, G.M. 2016 A nonlinear model for rotationally constrained convection with Ekman pumping. *J. Fluid Mech.* **798**, 50–87.

JULIEN, K., KNOBLOCH, E., RUBIO, A.M. & VASIL, G.M. 2012*a* Heat transport in low-Rossby-number Rayleigh–Bénard convection. *Phys. Rev. Lett.* **109** (25), 254503.

JULIEN, K., LEGG, S., MCWILLIAMS, J. & WERNE, J. 1996 Rapidly rotating turbulent Rayleigh–Bénard convection. *J. Fluid Mech.* **322**, 243–273.

JULIEN, K., RUBIO, A.M., GROOMS, I. & KNOBLOCH, E. 2012*b* Statistical and physical balances in low Rossby number Rayleigh–Bénard convection. *Geophys. Astrophys. Fluid Dyn.* **106** (4–5), 392–428.

KERR, R.M. 2001 Energy budget in Rayleigh–Bénard convection. *Phys. Rev. Lett.* **87**, 244502.

KING, E.M. & AURNOU, J.M. 2013 Turbulent convection in liquid metal with and without rotation. *Proc. Natl Acad. Sci. USA* **110** (17), 6688–6693.

KING, E.M., STELLMACH, S. & AURNOU, J.M. 2012 Heat transfer by rapidly rotating Rayleigh–Bénard convection. *J. Fluid Mech.* **691**, 568–582.

KING, E.M., STELLMACH, S., NOIR, J., HANSEN, U. & AURNOU, J.M. 2009 Boundary layer control of rotating convection systems. *Nature* **457** (7227), 301–304.

KOLHEY, P., STELLMACH, S. & HEYNER, D. 2022 Influence of boundary conditions on rapidly rotating convection and its dynamo action in a plane fluid layer. *Phys. Rev. Fluids* **7** (4), 043502.

KUNNEN, R.P.J. 2021 The geostrophic regime of rapidly rotating turbulent convection. *J. Turbul.* **22** (4–5), 267–296.

KUNNEN, R.P.J., GEURTS, B.J. & CLERCX, H.J.H. 2009 Turbulence statistics and energy budget in rotating Rayleigh–Bénard convection. *Eur. J. Mech. (*B*/Fluids)* **28** (4), 578–589.

KUNNEN, R.P.J., GEURTS, B.J. & CLERCX, H.J.H. 2010 Experimental and numerical investigation of turbulent convection in a rotating cylinder. *J. Fluid Mech.* **642**, 445–476.

KUNNEN, R.P.J., OSTILLA-MÓNICO, R., VAN DER POEL, E.P., VERZICCO, R. & LOHSE, D. 2016 Transition to geostrophic convection: the role of the boundary conditions. *J. Fluid Mech.* **799**, 413–432.

MAFFEI, S., CALKINS, M.A., JULIEN, K. & MARTI, P. 2019 Magnetic quenching of the inverse cascade in rapidly rotating convective turbulence. *Phys. Rev. Fluids* **4** (4), 041801.

MAFFEI, S., KROUSS, M.J., JULIEN, K. & CALKINS, M.A. 2021 On the inverse cascade and flow speed scaling behaviour in rapidly rotating Rayleigh–Bénard convection. *J. Fluid Mech.* **913**, A18.

MENEGUZZI, M. & POUQUET, A. 1989 Turbulent dynamos driven by convection. *J. Fluid Mech.* **205**, 297–318.

MOFFATT, K. & DORMY, E. 2019 *Self-Exciting Fluid Dynamos*. Cambridge University Press.

NASKAR, S. & PAL, A. 2022 Direct numerical simulations of optimal thermal convection in rotating plane layer dynamos. *J. Fluid Mech.* **942**, A37.

NIEVES, D., RUBIO, A.M. & JULIEN, K. 2014 Statistical classification of flow morphology in rapidly rotating Rayleigh–Bénard convection. *Phys. Fluids* **26** (8), 086602.

PAL, A. 2020 Deep learning emulation of subgrid-scale processes in turbulent shear flows. *Geophys. Res. Lett.* **47** (12), e2020GL087005.

PAL, A. & CHALAMALLA, V.K. 2020 Evolution of plumes and turbulent dynamics in deep-ocean convection. *J. Fluid Mech.* **889**, A35.

PAL, A., DE STADLER, M.B. & SARKAR, S. 2013 The spatial evolution of fluctuations in a self-propelled wake compared to a patch of turbulence. *Phys. Fluids* **25**, 095106.

PAL, A. & SARKAR, S. 2015 Effect of external turbulence on the evolution of a wake in stratified and unstratified environments. *J. Fluid Mech.* **772**, 361–385.

PLUMLEY, M. & JULIEN, K. 2019 Scaling laws in Rayleigh–Bénard convection. *Earth Space Sci.* **6** (9), 1580–1592.

PLUMLEY, M., JULIEN, K., MARTI, P. & STELLMACH, S. 2016 The effects of Ekman pumping on quasi-geostrophic Rayleigh–Bénard convection. *J. Fluid Mech.* **803**, 51–71.

PLUMLEY, M., JULIEN, K., MARTI, P. & STELLMACH, S. 2017 Sensitivity of rapidly rotating Rayleigh–Bénard convection to Ekman pumping. *Phys. Rev. Fluids* **2** (9), 094801.

RÜDIGER, G. & HOLLERBACH, R. 2006 *The Magnetic Universe: Geophysical and Astrophysical Dynamo Theory*. John Wiley & Sons.

RUBIO, A.M., JULIEN, K., KNOBLOCH, E. & WEISS, J.B. 2014 Upscale energy transfer in three-dimensional rapidly rotating turbulent convection. *Phys. Rev. Lett.* **112** (14), 144501.

SCHMITZ, S. & TILGNER, A. 2010 Transitions in turbulent rotating Rayleigh–Bénard convection. *Geophys. Astrophys. Fluid Dyn.* **104** (5–6), 481–489.

SCHWAIGER, T., GASTINE, T. & AUBERT, J. 2019 Force balance in numerical geodynamo simulations: a systematic study. *Geophys. J. Int.* **219** (Supplement_1), S101–S114.

SOWARD, A.M. 1974 A convection-driven dynamo. I. The weak field case. *Phil. Trans. R. Soc. Lond.* A **275** (1256), 611–646.

ST PIERRE, M.G. 1993 The strong field branch of the Childress–Soward dynamo. In *Solar and Planetary Dynamos* (ed. M.R.E. Proctor & A.D. Gilbert), pp. 245–277. Cambridge University Press.

STELLMACH, S. & HANSEN, U. 2004 Cartesian convection driven dynamos at low Ekman number. *Phys. Rev.* E **70** (5), 056312.

STELLMACH, S., LISCHPER, M., JULIEN, K., VASIL, G., CHENG, J.S., RIBEIRO, A., KING, E.M. & AURNOU, J.M. 2014 Approaching the asymptotic regime of rapidly rotating convection: boundary layers versus interior dynamics. *Phys. Rev. Lett.* **113** (25), 254501.

TARDUNO, J.A. 2018 Subterranean clues to the future of our planetary magnetic shield. *Proc. Natl Acad. Sci. USA* **115** (52), 13154–13156.

THELEN, J.-C. & CATTANEO, F. 2000 Dynamo action driven by convection: the influence of magnetic boundary conditions. *Mon. Not. R. Astron. Soc.* **315** (2), L13–L17.

TILGNER, A. 2012 Transitions in rapidly rotating convection driven dynamos. *Phys. Rev. Lett.* **109** (24), 248501.

TILGNER, A. 2014 Magnetic energy dissipation and mean magnetic field generation in planar convection-driven dynamos. *Phys. Rev.* E **90** (1), 013004.

TOBIAS, S.M. 2021 The turbulent dynamo. *J. Fluid Mech.* **912**, P1.

TOBIAS, S.M., CATTANEO, F. & BOLDYREV, S. 2012 MHD dynamos and turbulence. In *Ten Chapters in Turbulence* (ed. P.A. Davidson, Y. Kaneda & K.R. Sreenivasan), pp. 351–404. Cambridge University Press.

WEISS, S., STEVENS, R.J.A.M., ZHONG, J.-Q., CLERCX, H.J.H., LOHSE, D. & AHLERS, G. 2010 Finite-size effects lead to supercritical bifurcations in turbulent rotating Rayleigh–Bénard convection. *Phys. Rev. Lett.* **105** (22), 224501.

YAN, M. & CALKINS, M.A. 2022*a* Asymptotic behaviour of rotating convection-driven dynamos in the plane layer geometry. *J. Fluid Mech.* arXiv:2202.01382.

YAN, M. & CALKINS, M.A. 2022*b* Strong large scale magnetic fields in rotating convection-driven dynamos: the important role of magnetic diffusion. *Phys. Rev. Res.* **4** (1), L012026.

YAN, M., TOBIAS, S.M. & CALKINS, M.A. 2021 Scaling behaviour of small-scale dynamos driven by Rayleigh–Bénard convection. *J. Fluid Mech.* **915**, A15.